NUREG/CR-1072
EGG-2030
Distribution Category: R3

A STUDY OF MOLTEN DEBRIS FREEZING AND WALL EROSION IN THE RIA-ST-4 EXPERIMENT

Mohamed S. El-Genk
Richard L. Moore

Published April 1980

EG&G Idaho, Inc.
Idaho Falls, Idaho 83415

Prepared for the
U.S. Nuclear Regulatory Commission
Washington, D.C. 20
Under DOE Contract No. DE-AC07-76IDO1570
FIN No. A6041

ABSTRACT

The safe containment of molten debris following a hypothetical core meltdown accident in a light water reactor depends on the postaccident distribution and freezing of the debris. The objective of the present work is to analyze the freezing of molten debris produced during a severe, in-pile reactivity initiated accident experiment, designated RIA-ST-4. A one-dimensional physical model is developed to study the transient freezing of a molten debris layer (primarily a mixture of UO_2 and zircaloy) deposited on the inner surface of the RIA-ST-4 coolant flow shroud wall and to assess the potential for wall melting upon being contacted by the molten debris. The conditions of finite wall thickness, continuous cooling at the wall outer surface, radiative cooling of the debris, temperature-dependent thermophysical properties, and internal heat generation in the debris are considered in the analysis. The governing equations of this two-component, simultaneous freezing and melting problem in a finite geometry are solved numerically using a one-dimensional, finite element code based on the method of weighted residuals. Analyzed are the effects of molten debris temperature, radiative cooling at the debris layer surface, internal heat generation, zircaloy volume ratio within the debris, and initial wall temperature on the transient freezing of the debris and the potential melting of the wall.

SUMMARY

A UO_2 fuel rod, contained within a zircaloy flow shroud, was subjected to a single power burst which resulted in a total energy deposition (radially averaged at the axial flux peak location) of about 2930 J/g UO_2 (total enthalpy of about 2220 J/g UO_2) during the Reactivity Initiated Accident-Scoping Test-4 (RIA-ST-4) conducted in the Power Burst Facility (PBF) at the Idaho National Engineering Laboratory. This energy deposition is well above what is expected during a postulated control rod dropout (boiling water reactor) or ejection (pressurized water reactor) accident in a light water reactor. The RIA-ST-4 experiment was performed to quantify the magnitude of any pressure pulses which might occur in the PBF as a result of a severe fuel rod failure.

The test rod failed 33 ms after the initiation of the burst, which lasted about 76 ms, at a total energy deposition of about 1550 J/g UO_2 (the total enthalpy was about 1465 J/g UO_2). Extensive amounts of molten fuel and cladding were produced and ejected axially and radially within the test shroud upon rod failure. Molten debris that was ejected upward froze and formed a complete flow blockage at the exit of the shroud. The inner surface of the zircaloy-4 shroud wall was completely coated with a debris layer having a thickness of about 0.7 mm. However, the inner surface of the wall (melting point of ~2100 K) did not melt upon contact by the molten debris, which is primarily a mixture of UO_2 fuel and zircaloy cladding (melting point of UO_2 ~3113 K). The objectives of the present analysis are to (a) study the transient freezing of the molten debris layer deposited on the inner surface of the RIA-ST-4 shroud wall upon test fuel rod failure, and (b) assess the potential for wall erosion due to melting upon being contacted by the molten debris.

A physical model is developed to study the transient freezing of the molten debris layer on the shroud wall, which had a finite thickness of 3.05 mm and was continuously cooled at its outer surface by coolant bypass flow. To simplify the analysis, molten debris is treated as a homogeneous mixture of UO_2 and zircaloy, despite the fact that molten UO_2 and zircaloy could form a solid solution(s) which will freeze at a lower temperature than that of UO_2. This simplifying assumption is considered because the thermophysical properties of such a solid solution(s) are not reported in the literature, and the freezing temperature is dependent on the molar percentage of the consitituents (that is, UO_2 and zircaloy).

The governing equations of this two-component, simultaneous freezing and melting problem in a finite geometry are solved numerically using a one-dimensional, finite element code (SINGLE) based on the method of weighted residuals. The conditions of finite wall thickness, continuous cooling at the wall outer surface, radiative cooling at the molten debris layer surface, temperature-dependent thermophysical properties, and internal heat generation in the debris are considered in the analysis.

Results indicated that the transient freezing of the molten debris layer is controlled by the transient heat conduction through the wall and the radiative cooling at the debris layer surface. The molten debris temperature, the internal heat generation in the debris, the zircaloy volume ratio within the debris, and the initial wall temperature strongly influence the debris freezing and the potential melting of the wall. Cooling the debris by radiation reduces the total freezing time of the debris layer. Increasing the molten debris temperature or the internal heat generation, however, increases the total freezing time of the debris layer. Increasing the zircaloy volume ratio within the debris increases the effective thermal conductivity, and thus significantly reduces the total freezing time of the debris layer.

The calculated temperature-time history at the shroud wall outer surface is employed to estimate the thicknesses of the ZrO_2 and the oxygen-stabilized alpha-zircaloy layers that were formed at the shroud wall outer surface due to the steam-zircaloy reaction during film boiling. From the agreement of the calculated thicknesses with the measured values, it is deduced that the total fuel enthalpy at the time of rod failure was about 1460 ± 60 J/g UO_2. This fuel enthalpy is almost the same as that calculated from the energy deposition in the test fuel rod at the time of rod failure (~1465 J/g UO_2).

The calculations indicated that the RIA-ST-4 shroud wall should not melt upon contact by the molten debris because of the low temperatures of the wall (538 K) and of the debris (3500 K) at the time of contact (rod failure time). This is in agreement with the experimental data. However, melting of the wall would occur if the initial wall temperature was higher than 1000 K, and the molten debris temperature was in excess of 3500 K. Melting of the wall would be unstable under such conditions, that is, a molten layer would grow into the wall until it reached a maximum thickness, which could be less than the initial thickness of the wall; then the molten layer would thin by freezing and eventually disappear. The maximum melting of the wall and the total lifetime of the wall molten layer depend on the radiative cooling at the debris layer surface, the internal heat generation in the debris, and the molten debris and wall temperatures at the time of contact. It should be noted that radiative cooling at the debris layer surface strongly influences the transient growth (melting) and decay (freezing) of the wall molten layer. The cooling of the debris by thermal radiation reduces the maximum melting of the wall and decreases the total lifetime of the wall molten layer.

The agreement between the calculations and experimental results supports the validity of the physical model and the analytical approach presented in this work. In particular, the following conclusions are drawn from this agreement:

1. The treatment of molten debris as a homogeneous mixture of UO_2 fuel and zircaloy cladding, in which the thermophysical properties are assessed in terms of those of the constituents, is a reasonable assumption.

2. The analysis of transient freezing of molten debris on cold core structures following a hypothetical core meltdown accident in a light water reactor should consider the effect of thermal radiation in cooling the debris rather than transient conduction.

3. In the RIA-ST-4 experiment, the rate of energy deposition in the debris layer (expressed in Joules per gram of UO_2 per megawatt second of the transient core energy) was no more than 20% higher than that in the test rod before failure.

CONTENTS

FIGURES

TABLES

NOMENCLATURE

a	molten debris layer thickness (m)
b	shroud wall thickness (m)
B	time constant (s^{-1}), Equation (1)
c	heat capacity (J/kg·K)
h	heat transfer coefficient ($W/m^2 \cdot K$)
I	fuel enthalpy (J/kg)
k	thermal conductivity (W/m·K)
L	latent heat of fusion (J/kg)
Q	fission heating rate (W/g UO_2), Equation (1)
Q_o	fission heating rate at time of rod failure (W/g UO_2), Equation (1)
t	time (s)
T	temperature (K)
T_{crit}	critical temperature of the coolant (K)
T_f	fusion temperature (K)
r	coordinate (m)

Greek Letters

α	thermal diffusivity (m^2/s)
δ	frozen debris crust thickness
δ_m	wall molten layer thickness
ε	zircaloy volume ratio in the debris
ν	energy deposition weight factor, Equation (1)

Subscripts

a	at the molten debris layer surface (r = a)
b	at the shroud wall outer surface (r = -b)
B	film boiling
c	convective cooling, coolant bypass flow
D	molten debris at the time of rod failure
f	UO_2 fuel, fusion
I	wall inner surface
m	wall molten layer
mf	molten fuel
mp	wall melting point
o	initially (at the time of rod failure)
R	radiative cooling
s	debris layer
sf	solid fuel
UO_2	uranium dioxide
Zr	zircaloy
w	solid wall

A STUDY OF MOLTEN DEBRIS FREEZING AND WALL EROSION IN THE RIA-ST-4 EXPERIMENT

1. INTRODUCTION

It is important to light water reactor (LWR) safety analysis to understand the transient freezing of molten debris on cold core structures following a hypothetical core meltdown accident. The purpose of the present work is to study the transient freezing of a molten debris layer (primarily a mixture of UO_2 fuel and zircaloy cladding) deposited on the inner surface of the test shroud wall during a severe reactivity initiated accident (RIA) in-pile experiment (RIA-ST-4) and to assess the potential for wall erosion due to melting (melting point of the wall $\sim$2100 K) upon being contacted by the molten debris (melting point of $UO_2 \sim$3100 K).

A single, unirradiated, UO_2 fuel rod, contained within a zircaloy flow shroud, was subjected to a single power burst which deposited a total energy (radially averaged at the axial flux peak location) of about 2930 J/g UO_2 (total enthalpy of 2220 J/g UO_2) during the RIA-ST-4 experiment.[1,2] This energy deposition is well above what is possible during a hypothetical control rod ejection accident in a commercial LWR. The purpose of the RIA-ST-4 experiment was to quantify the magnitude of any pressure pulses which might occur in the Power Burst Facility due to a severe rod failure. The performance of such an in-pile experiment, however, has provided important information with regard to molten debris movement, relocation, and freezing on cold walls.

The test fuel rod failed approximately 33 ms after the initiation of the burst, which lasted about 76 ms, when the total energy deposition (radially averaged at the axial flux peak location) was about 1550 J/g UO_2 (total enthalpy was about 1465 J/g UO_2). Upon fuel rod failure, extensive amounts of molten debris were produced and expelled axially and radially within the zircaloy-4 flow shroud. A molten debris layer having a thickness of about 0.7 mm was deposited on the inner surface of the shroud wall. The shroud wall had a finite thickness (3.05 mm) and was continuously cooled at its outer surface by coolant bypass flow.

A physical model is developed to (a) study the transient freezing of the molten debris layer on the inner surface of the RIA-ST-4 shroud wall; and (b) assess the conditions for potential wall melting upon contact by molten debris. The conditions of finite wall thickness, continuous cooling at the wall outer surface, radiative cooling at the molten debris layer surface, temperature-dependent thermophysical properties, and internal heat generation in the debris are considered in the analysis.

The exact analytical solutions of transient heat conduction problems with a moving phase-transformation boundary are only available for those cases with simplified boundary conditions, such as constant temperature,[3,4] constant heat flux,[5] or a semi-infinite geometry.[3,6] The difficulty arises from the nonlinearity of the boundary at the moving change-of-phase front(s). In addition, the governing equations become nonhomogeneous and nonlinear when internal heat generation and temperature-dependent thermophysical properties are considered, which is the case in the present investigation. The exact analytical solution of the freezing of a stagnant, superheated liquid on a semi-infinite wall that undergoes simultaneous melting has been introduced by Epstein.[6] In his analysis, the freezing crust and the wall molten layer grew at a parabolic rate. The freezing and melting coefficients were solely dependent on the thermophysical properties and the initial temperatures of the wall and the freezing liquid.

Recently, the transient freezing of a flowing liquid on the inside surface of a finite wall that is melting simultaneously and being convectively cooled at its outer surface has been analyzed.[7] Because of the convective boundary conditions at the freezing front and at the wall outer surface and the finite thickness of the wall, the freezing crust and the wall molten layer were unstable. They

continued to grow until they either reached a maximum thickness and then became thinner or approached a steady state. The maximum thickness and total lifetime of the frozen crust and the wall molten layer depend on the wall thickness, the thermophysical properties, the cooling conditions at the wall outer surface, and the initial temperatures of the wall and the freezing liquid.

The previous work[3-7] considered the freezing of a pure, single liquid rather than a mixture of two liquids of different freezing properties, which is the case in the present investigation. An exact analytical solution of the present problem, which consists of two components (UO_2 and zircaloy) and simultaneous freezing and melting in a finite geometry, is impossible because of the nonhomogeneous, nonlinear governing equation due to the internal heat generation in the debris and the temperature-dependent thermophysical properties, respectively, the nonlinearity of the boundary conditions at the change-of-phase front(s), the radiative cooling at the debris layer surface, and the finite thickness of the wall; however, numerical solutions are available.

The governing equations of the present physical model of two-component freezing and melting in a finite geometry are solved using a finite element code based on the method of weighted residuals. Parametric analysis is performed to evaluate the effects of molten debris temperature, radiative cooling, internal heat generation in the debris, zircaloy volume ratio within the debris, and initial wall temperature on the transient freezing of the molten debris layer and the potential erosion of the wall due to melting.

A summary of the RIA-ST-4 experiment design, conduct, and results is presented. A physical model is developed to study the transient freezing of the molten debris layer on the inner surface of the RIA-ST-4 shroud wall and to assess the potential erosion of the wall due to melting. A parametric analysis is performed, and conclusions are presented. Supporting analyses are contained in the appendices.

2. EXPERIMENT DESIGN, CONDUCT, AND RESULTS

A series of tests are being conducted in the Power Burst Facility (PBF) at the Idaho National Engineering Laboratory to study the behavior of a single rod or small clusters of fuel rods during a postulated reactivity initiated accident, simulating a hypothetical control rod ejection accident in a commercial boiling water reactor (BWR). The objectives of these tests are to define an energy deposition failure threshold and to determine modes and consequences of fuel rod failure as functions of the increase in fuel enthalpy during the burst, the irradiation history of the fuel, and the fuel rod design. The test conditions are typical of a hot startup in a commercial BWR (that is, coolant pressure of 6.45 MPa, coolant temperature of 538 K, and coolant flow rate of 0.085 l/s) in order to simulate the most severe RIAs postulated.

2.1 Experiment Design

The Reactivity Initiated Accident-Scoping Test-4 (RIA-ST-4) was conducted to quantify the magnitude of potential pressure pulses that might occur in the PBF as a result of a severe fuel rod failure. The PBF consists of an open tank reactor vessel; a driver core region; a canal for transfer and temporary storage of PBF fuel and test fuel assemblies; a central flux trap region in which an in-pile tube is located; and a pressurized water flow loop. This flow loop permits the control of the coolant environment conditions (flow rate, temperature, and pressure) to the test fuel rod(s) to be indicative of those in commercial LWRs.

The PBF nuclear core is a right-circular annulus, 1.3 m in diameter and 0.914 m in length, encompassing a centrally located vertical flux trap, 0.21 m in diameter. The core contains eight control rods for reactivity control during steady state operation, and four additional transient rods which dynamically control the reactivity in the core during power burst operation. Each of the control and transient rods consists of a stainless steel canister which contains a cylindrical annulus of boron carbide and is operated in an air-filled shroud; a cut-away view of the PBF reactor is shown in Figure 1.

The PBF driver core is cooled by water from a low pressure primary coolant system. Coolant,

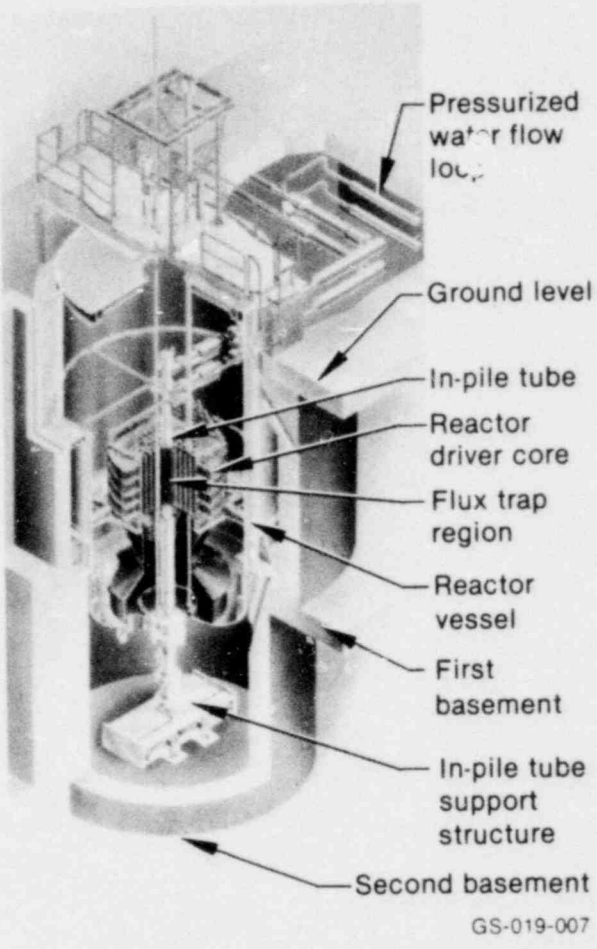

Figure 1. Power Burst Facility reactor cut-away view.

provided by two primary coolant pumps, flows through the core at a rate of 0.946 m^3/s. The PBF reactor operates in three modes: (a) a steady state mode with power levels up to 28 MW; (b) a natural power burst mode with a reactor period as short as one millisecond and peak power as high as 270 GW; and (c) a shaped burst that could provide various energy densities in the test rod(s) to simulate many types of postulated reactor accidents.

The in-pile tube (IPT) is a thick-walled Inconel 718, high strength pressure tube designed to accommodate a pressure pulse of up to 51.7 MPa above the steady state pressure in the coolant loop system without damage to the driver core. A zircaloy-4 flow tube is positioned inside the IPT to direct the coolant flow. Coolant enters through an inlet nozzle at the top of the IPT above

the reactor core and flows down the annulus between the IPT wall and the bypass flow tube. It then reverses at the bottom of the flow tube, just above a catch basket, and passes up through both the central region of the bypass flow tube and through the test shroud to cool the test fuel rod(s). The flow exits above the reactor core through the IPT outlet nozzle.

The RIA-ST-4 experiment consisted of a single UO_2 fuel rod contained within a zircaloy flow shroud. The design characteristics of the rod, the test shroud, and the bypass flow tube are listed in Table 1. The experiment was instrumented for measurement of the shroud coolant temperature, pressure, and flow rate. No instrumentation was installed on the test fuel rod. The RIA-ST-4 test train is illustrated in Figure 2, indicating the approximate location of the instrumentation. Details of the test instrumentation and experimental results are described elsewhere.[1,2]

As shown in Figure 3, which presents an axial cross section of the RIA-ST-4 fuel rod assembled

Table 1. Design characteristics of test fuel rod, flow shroud, and bypass flow tube

Fuel	
Material	UO_2
Pellet outside diameter (mm)	9.3
Pellet length (mm)	15.49
Pellet enrichment (wt% ^{235}U)	20
Density (% of theoretical)	93
Fuel stack length (m)	0.914
Pellet end configuration	Dished
Burnup	Unirradiated
Cladding	
Material	Zircaloy-4
Outside diameter (mm)	10.73
Wall thickness (mm)	0.61
Fuel Rod	
Overall length (m)	1.0
Fill gas	Helium
Cold internal pressure (MPa)	3.79
Diametral gap width (mm)	0.105
Test Shroud	
Material	Zircaloy-4
Shroud inside diameter (mm)	19.3
Shroud outside diameter (mm)	25.4
Coolant flow rate during the burst (l/s)	0.085
Coolant velocity (m/s)	0.42
Bypass Flow Tube	
Material	Zircaloy-4
Tube inside diameter (mm)	120.65
Tube outside diameter (mm)	127
Coolant flow rate during the burst (l/s)	~1.1
Coolant velocity (m/s)	~0.1

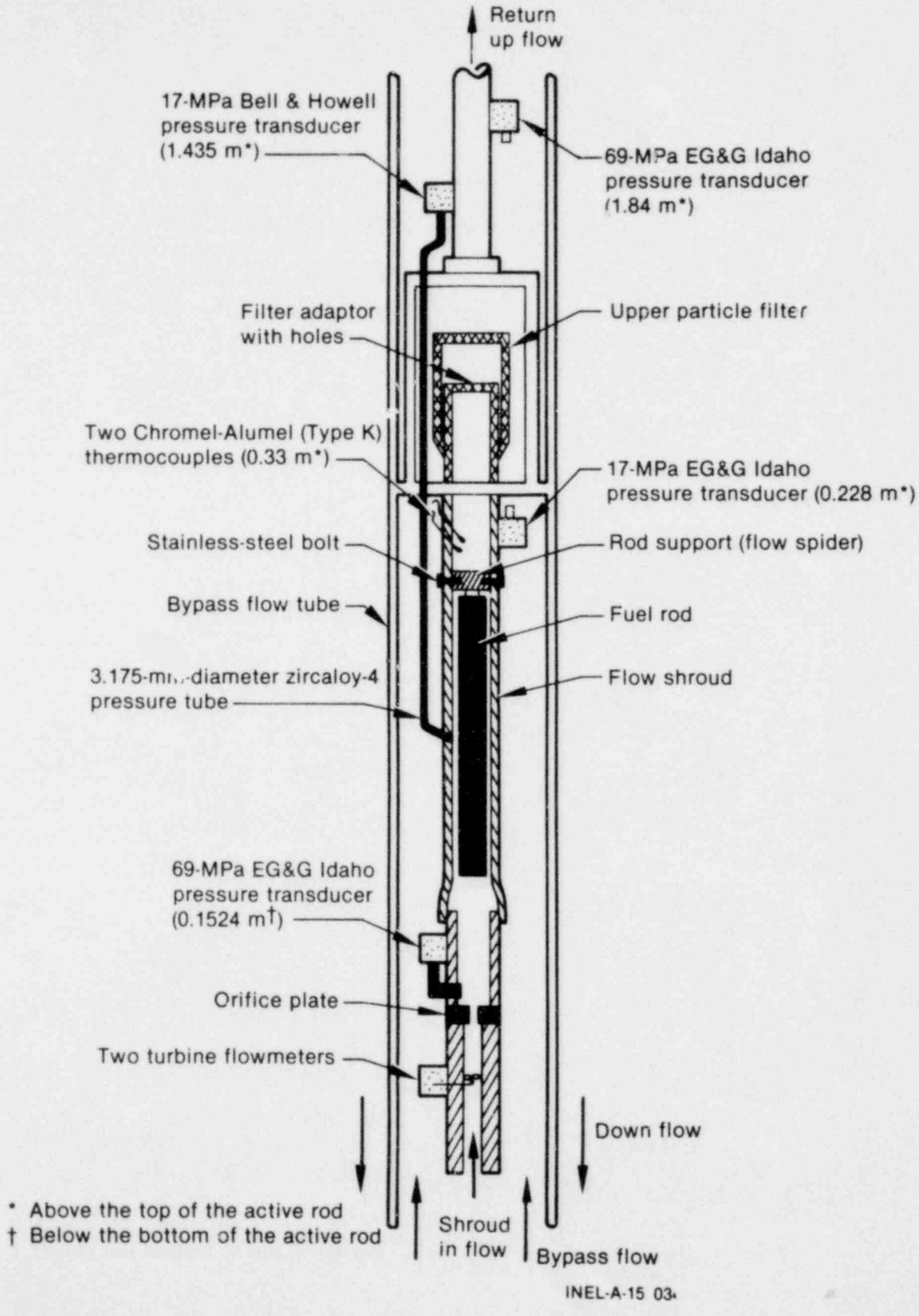

Figure 2. **Diagram of RIA-ST-4 test train.**

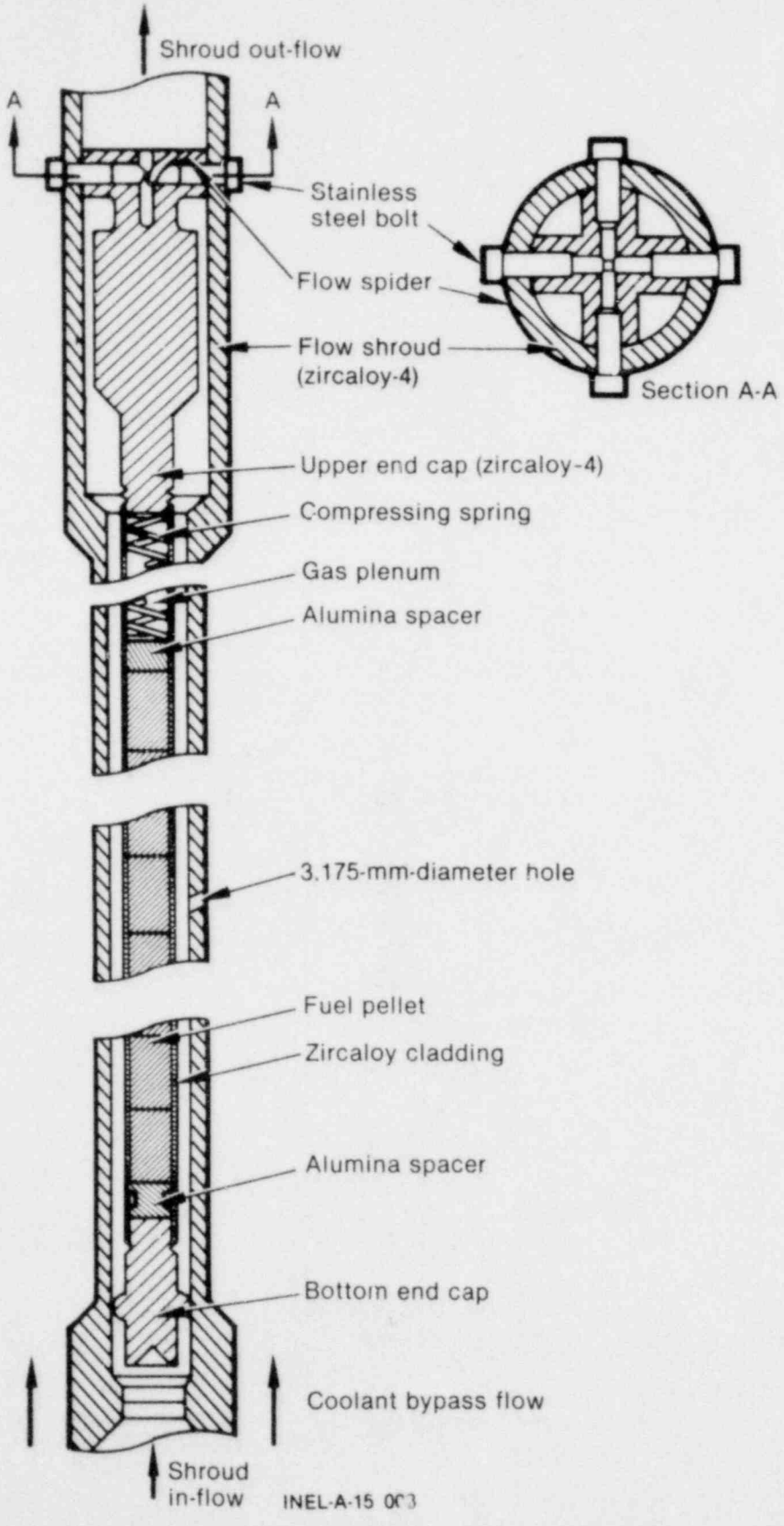

Figure 3. **Axial cross section of RIA-ST-4 fuel rod assembled in flow shroud.**

in the flow shroud, the top of the test fuel rod was rigidly secured to the shroud wall by four stainless steel bolts (flow spider), with the rod free to expand axially downward. A 3.175-mm-diameter hole was made in the shroud wall at the axial flux peak location to attach a pressure tube, so that the coolant pressure inside the shroud could be measured at this location (see Figure 2).

2.2 Experiment Conduct

The RIA-ST-4 experiment consisted of three phases; a heatup, a power calibration, and a power burst. During the heatup phase, the coolant conditions were established at 538 K for the inlet temperature, 6.45 MPa for the pressure, and 0.760 l/s for the shroud coolant flow rate, which were maintained through the power calibration phase of the test. The power calibration was performed to compare the steady state power of the test fuel rod calculated from the thermal-hydraulic balance across the flow shroud with the rod power determined by the reactor neutron detector chambers and the self-powered neutron detectors (SPNDs) mounted on the test train.

During the power burst, the coolant conditions were kept the same as in the previous phases of the test except for the shroud coolant flow rate which was reduced to 0.085 l/s. The test fuel rod was subjected to a single power burst which lasted a total of about 76 ms. A reactor peak power of 15.9 GW was achieved approximately 30 ms after the initiation of the burst. The experimental results are briefly discussed in the following section.

2.3 Experiment Results

The total energy deposition in the RIA-ST-4 fuel rod during the power burst was about 2930 J/g UO_2 (total enthalpy about 2220 J/g UO_2), radially averaged at the axial flux peak location. The rod failed approximately 33 ms after the initiation of the burst (3 ms after the peak power occurred), when the total energy deposition was about 1550 J/g UO_2. The total enthalpy at the time of failure was about 1465 J/g UO_2, which is less than the total energy deposition because of heat transfer to the cladding and the coolant during the burst.

The generation of coherent pressure pulses up to 35 MPa in the test shroud due to an energetic molten fuel-coolant interaction (MFCI)[8] indicated rod failure. However, the coolant pressure in the bypass flow tube only increased about 2 MPa during the experiment. The average temperature of the fuel at the time of failure is estimated to have been about 3500 K (~400 K above the melting point of UO_2). At this temperature, the contribution to the pressure by the UO_2 fuel vapor is negligibly small, about 0.05 MPa.[9] There were no measurements of coolant temperature at the inlet of the shroud because the thermocouples at this location failed before the burst. The two thermocouples located 0.33 m above the top of the active fuel rod recorded coolant temperatures in excess of 940 K.

Extensive amounts of molten fuel and cladding were produced and expelled axially and radially within the shroud upon rod failure due to the high internal pressure in the fuel rod at the time of failure. The outer diameter of the shroud was enlarged from 25.4 to approximately 27.66 mm. This deformation was apparently caused by the pressure pulses generated within the shroud, together with the wall overheating induced by the deposited molten debris on the inner surface of the shroud wall.

A total of 155 g of molten debris were fragmented into fine particles upon contact with the coolant. Approximately 58% of this amount (~90 g) was fragmented into particles ranging from 38 to 2000 μm in diameter, which is characteristic of particle sizes generally observed in MFCI events.[10] The particles were typically spherical or round, with predominantly smooth surfaces, indicating that the fragmentation occurred when the debris was molten.[8] A few unmelted chunks of UO_2 fuel were observed in the debris, revealing that fuel pellets at the extreme ends of the active fuel stack did not melt completely before rod failure. However, melting of the fuel might have continued even after rod failure due to the energy deposition in the dispersed fuel fragments during the remainder of the power burst. The energy deposition during this period (~45 ms) was estimated to have been about 1380 J/g UO_2.

A pressure transducer (17-MPa Bell and Howell pressure transducer) was connected via a small zircaloy pressure tube (3.175 mm in diameter) installed through a hole in the test shroud wall (see Figures 2 and 3) to measure the coolant pressure in the shroud. Upon rod failure, the molten debris filled the entrance of the connecting tube, which

eventually failed due to melting. The molten debris was then splashed out on the shroud wall outer surface, as shown in Figure 4. The lower portion of the pressure tube became detached first, as evidenced by the downward expulsion of the molten debris on the wall surface. The enlargement of the original hole in the wall by ablation is also evident.

The molten debris that was ejected axially upward upon rod failure, passing through the spider flow area at the top of the rod, was deposited on the inner surface of the flow shroud causing a partial blockage of the flow, as shown in Figure 5. A part of this debris accumulated on the top of the flow spider as shown in Figure 6, which presents a transverse section in the flow spider region before and after the RIA-ST-4 experiment. A radial cross section of the flow spider before and after the test is shown in Figure 7. As indicated, the accumulated debris on the top of the flow spider filled the open axial and inclined holes in the spider region, causing extensive melting of the stainless steel bolts. The continuous freezing of the molten debris at the exit of the flow shroud induced a complete flow blockage of the shroud, as is indicated in Figure 5.

The inner surface of the shroud wall was extensively coated with a layer of molten debris as shown in Figure 5, which shows the upper two thirds of the split shroud and radial cross sections at both ends of the upper third of the shroud. Shown in Figure 8 are two sections of the

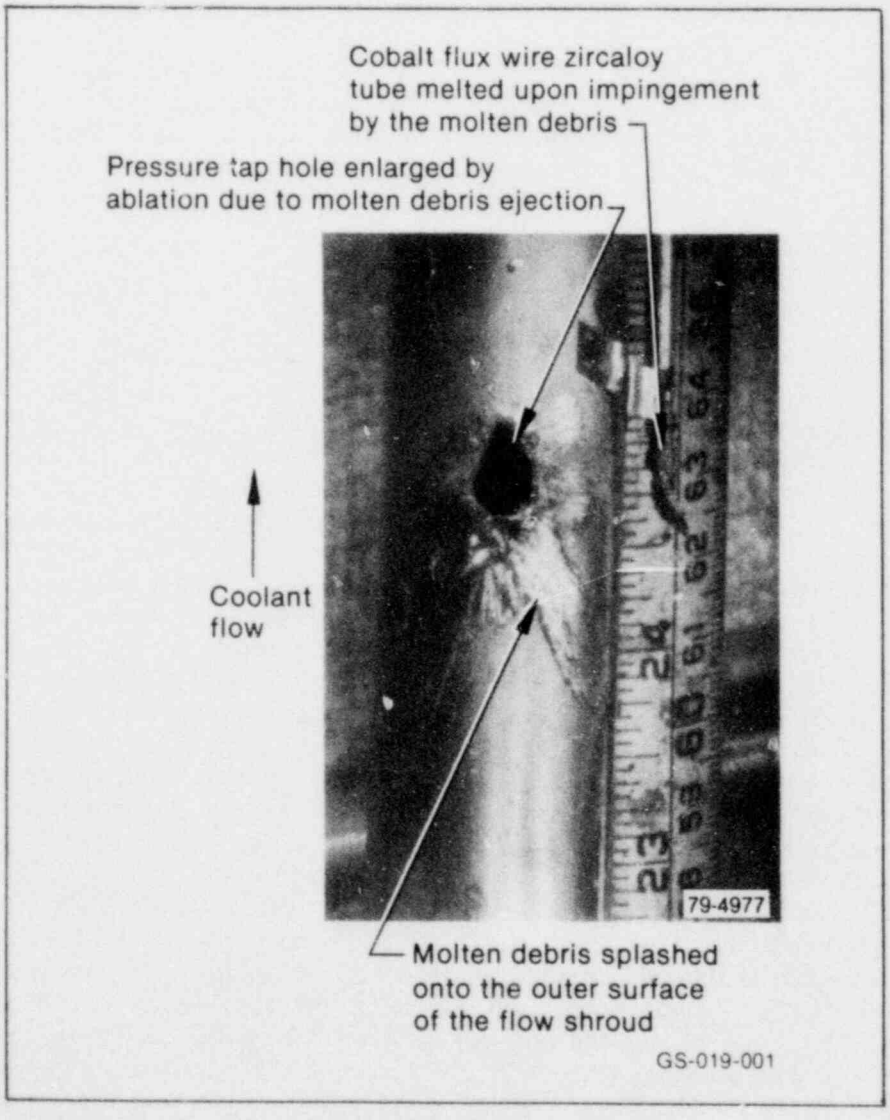

Figure 4. Molten fuel debris ejected through pressure tap hole.

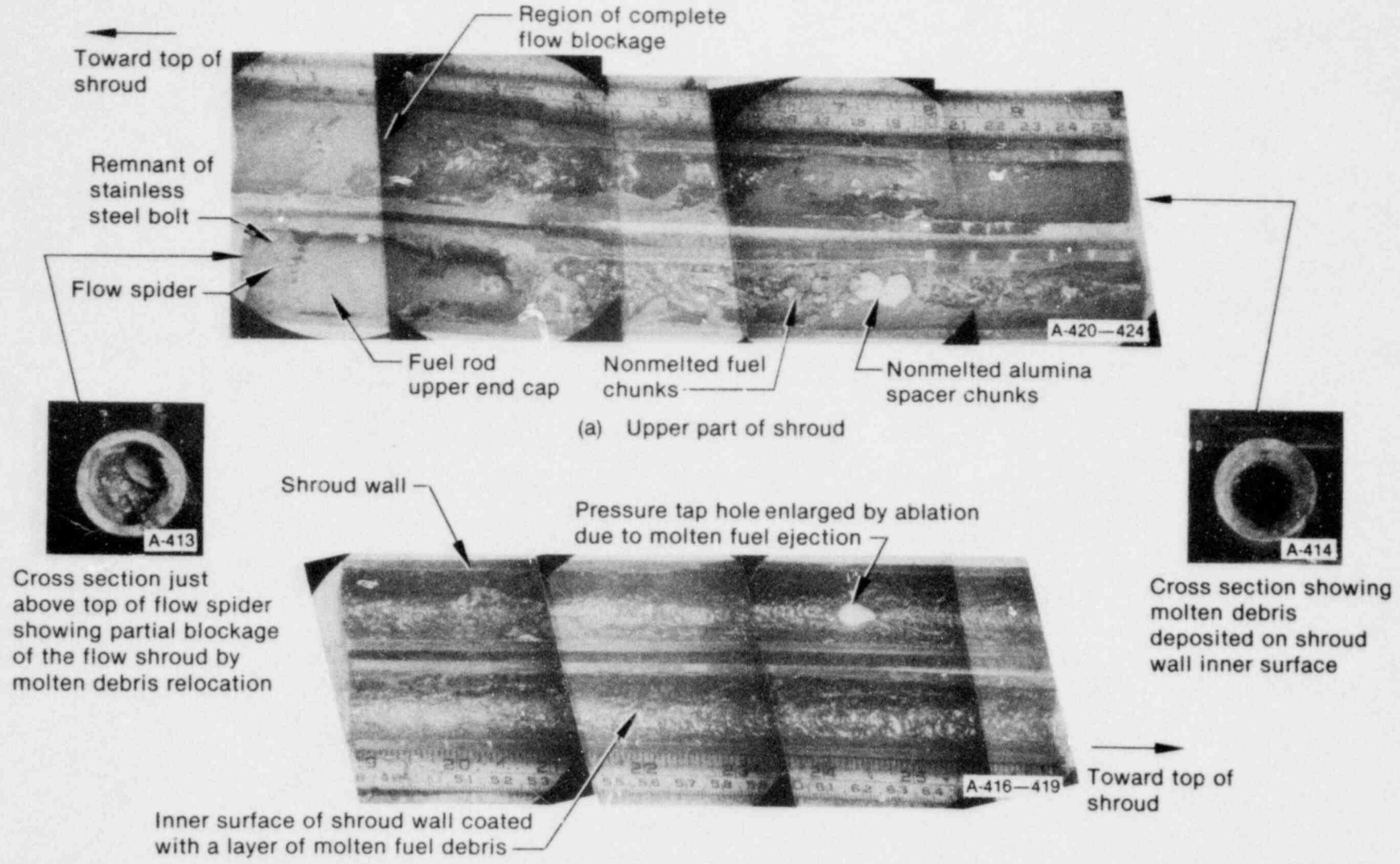

Figure 5. Flow shroud split to show molten debris deposited on inner surface.

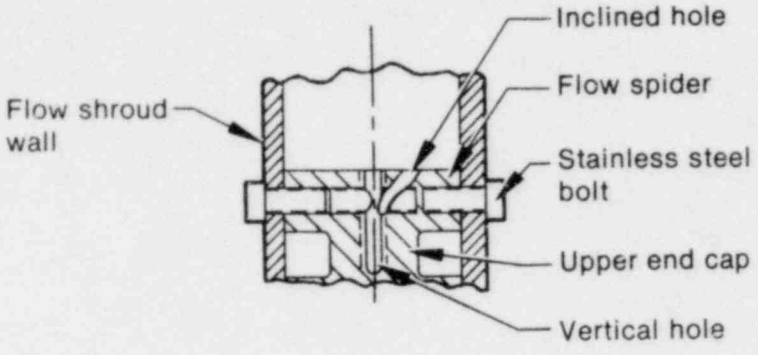

(a) Before the burst

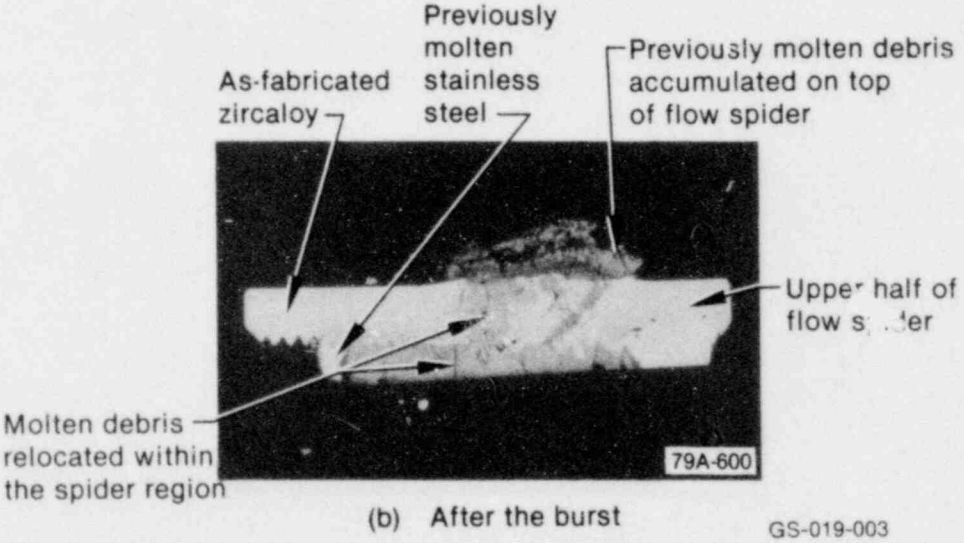

(b) After the burst

GS-019-003

Figure 6. Molten debris accumulated on top of flow spider.

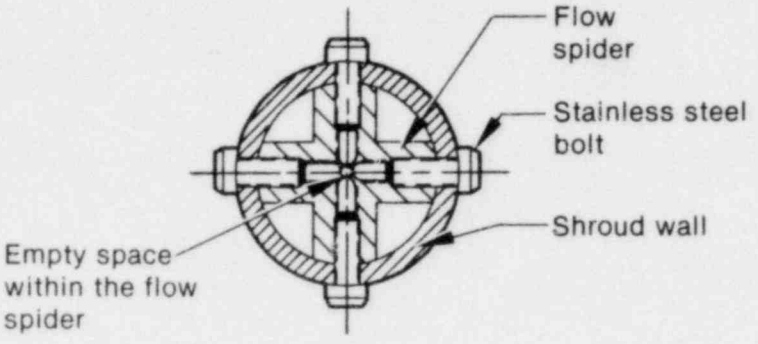

(a) Before the burst

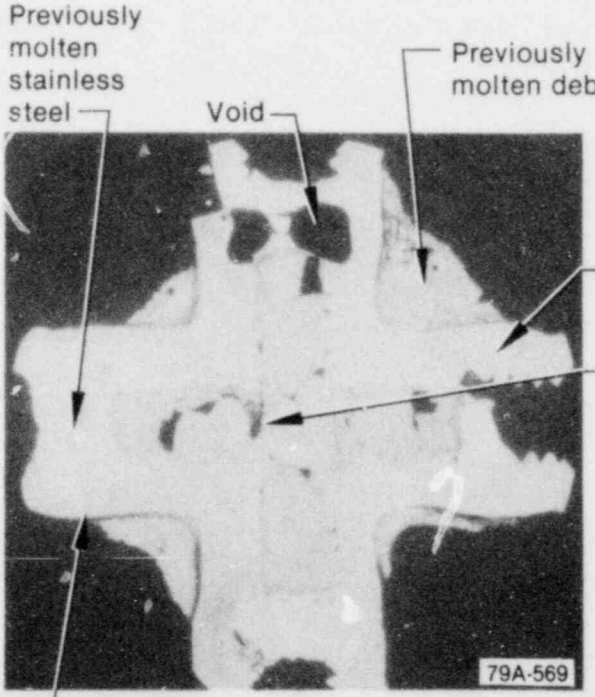

GS-019-004

(b) After the burst

Figure 7. Molten debris relocation and freezing within the flow spider.

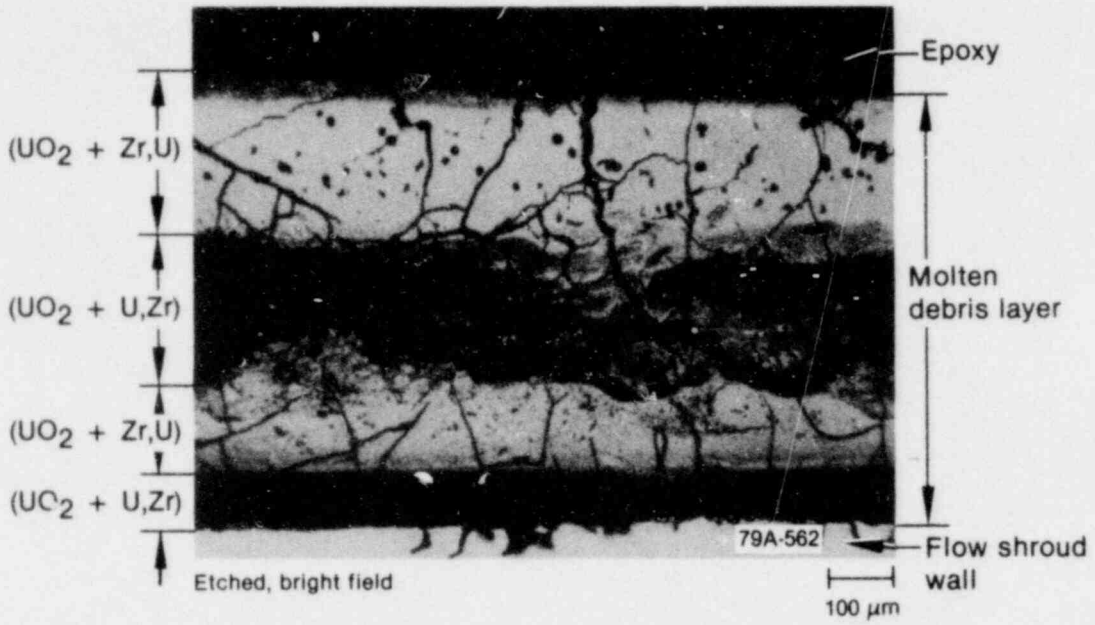

(a) 0.13 m above the bottom of fuel stack

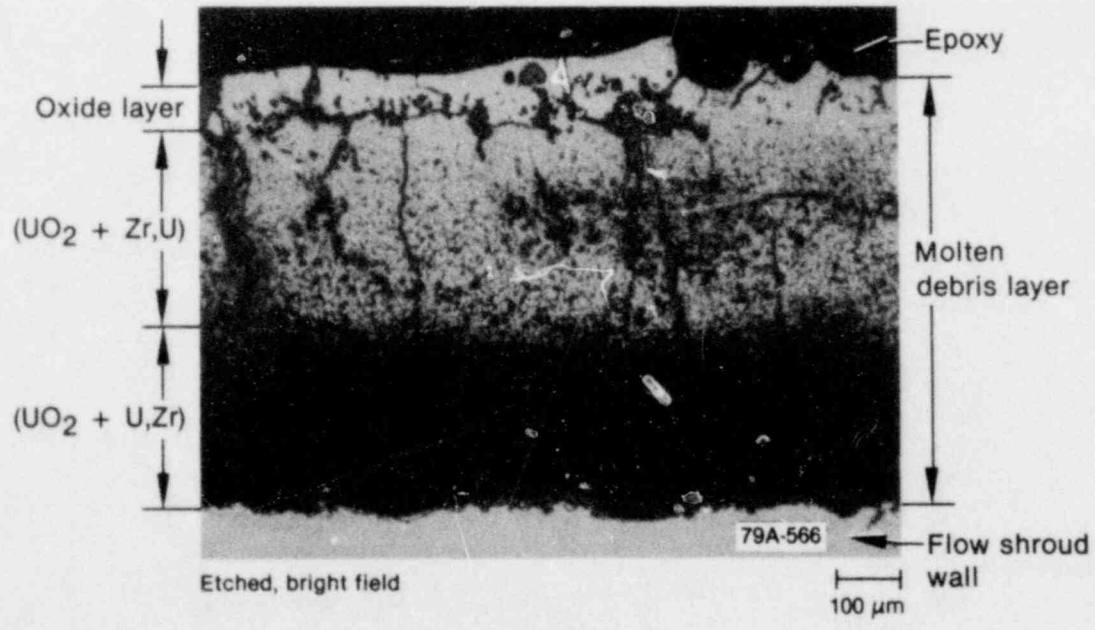

(b) 0.344 m above the bottom of fuel stack

GS-019-005

Figure 8. Molten debris layer deposited on inner surface of shroud wall.

deposited molten debris layer at two different axial locations, 0.13 and 0.344 m above the bottom of the fuel stack. The deposited debris layers were of the same thickness at both locations (about 0.7 mm), but of different metallurgical compositions. Extensive oxidation of the debris layer surface due to molten debris-steam reaction is evident in Figure 8(b). The compositions of the debris layer indicated in Figure 8 were deduced from metallographic examination.[2] The total amount of molten debris deposited onto the inner surface of the shroud wall is estimated to have been about 386 g, which represents approximately 51% of the total mass of UO_2 fuel (634 g) and zircaloy cladding (115 g) present in the test fuel rod.

The inner surface of the RIA-ST-4 shroud wall did not melt upon being contacted by the molten debris. However, ZrO_2 and oxygen-stabilized alpha-zircaloy layers were formed on the shroud wall outer surface due to the zircaloy-steam reaction during film boiling.[11,12] The interaction between the molten debris (mostly UO_2) and the wall (zircaloy-4) produced an oxygen-stabilized alpha-zircaloy layer at the shroud wall inner surface.[13,14] Figure 9, which presents cross-sectional views of the shroud wall, illustrates the reaction layer microstructures at the inner and outer surfaces of the wall. Details of the metallurgical examination results are described elsewhere.[2]

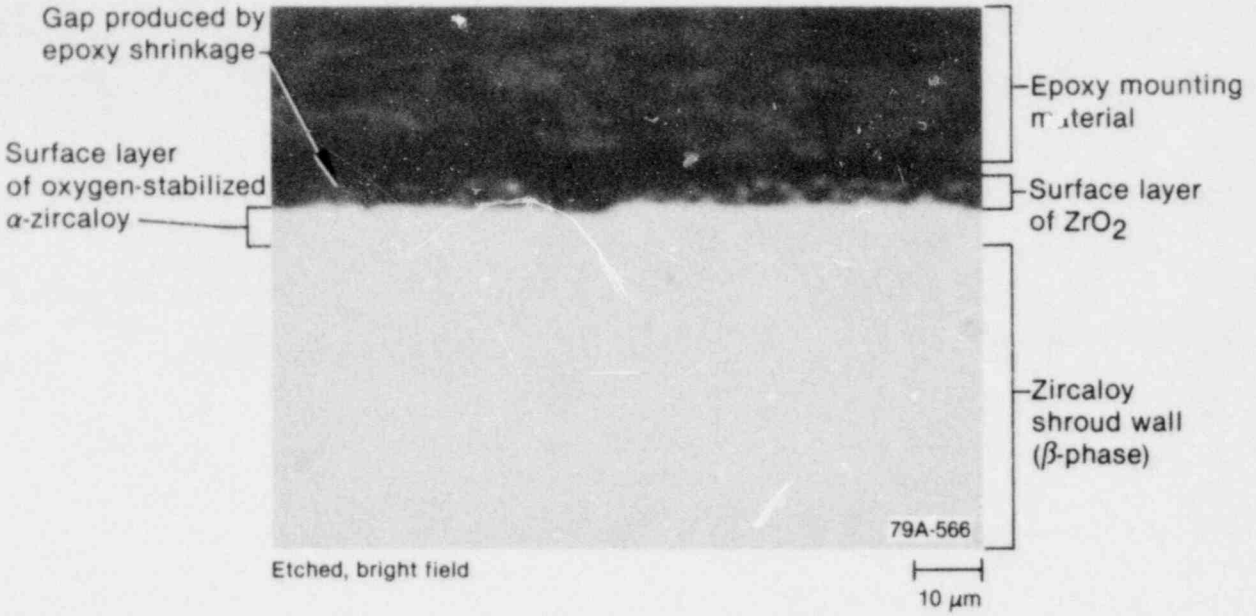

(a) Outer surface of shroud wall

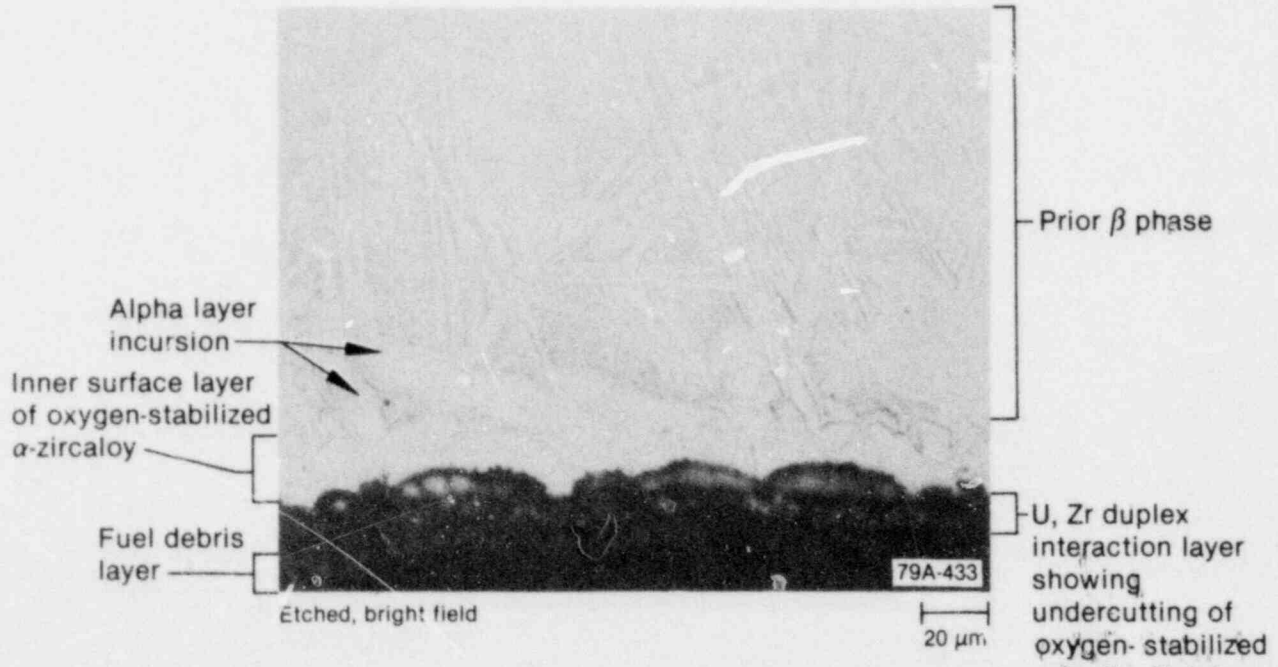

(b) Inner surface of shroud wall

GS-019-006

Figure 9. Reaction layer microstructures at inner and outer surfaces of shroud wall.

3. FREEZING OF MOLTEN DEBRIS ON THE INNER SURFACE OF THE RIA-ST-4 SHROUD WALL

In this section, the transient freezing of a molten debris layer on the inner surface of the RIA-ST-4 shroud wall is analyzed and the potential for wall melting is assessed. The molten debris layer, primarily a mixture of UO_2 and zircaloy, had a thickness of about 0.7 mm, whereas the shroud wall had a thickness of 3.05 mm and was continuously cooled at its outer surface by coolant bypass flow. The purpose of the present analysis is to develop a physical model to study this two-component, simultaneous freezing and melting problem in a finite geometry. Considered here are the conditions of finite wall thickness, continuous cooling at the shroud wall outer surface, radiative cooling at the debris layer surface, internal heat generation in the debris, and temperature-dependent thermophysical properties. Discussed are the effects of molten debris temperature, radiative cooling of the debris, internal heat generation, zircaloy volume ratio within the debris, and initial wall temperature on the transient freezing of the debris layer and the potential for wall erosion due to melting.

3.1 Physical Model

A representation of the physical model is presented in Figure 10. At time zero (rod failure time), a molten debris layer having a thickness 'a' was plated on the inner surface, r = 0, of the test shroud wall. The shroud wall had a finite thickness 'b' and was initially at a uniform temperature, T_c, equal to that of the coolant flowing along the outer surface of the wall, r = -b. The temperature of the molten debris, T_D, was initially higher than the fusion temperature of the UO_2 fuel, $T_{f_{UO_2}}$, and of the zircaloy cladding, $T_{f_{Zr}}$. Should the temperature at the inner surface

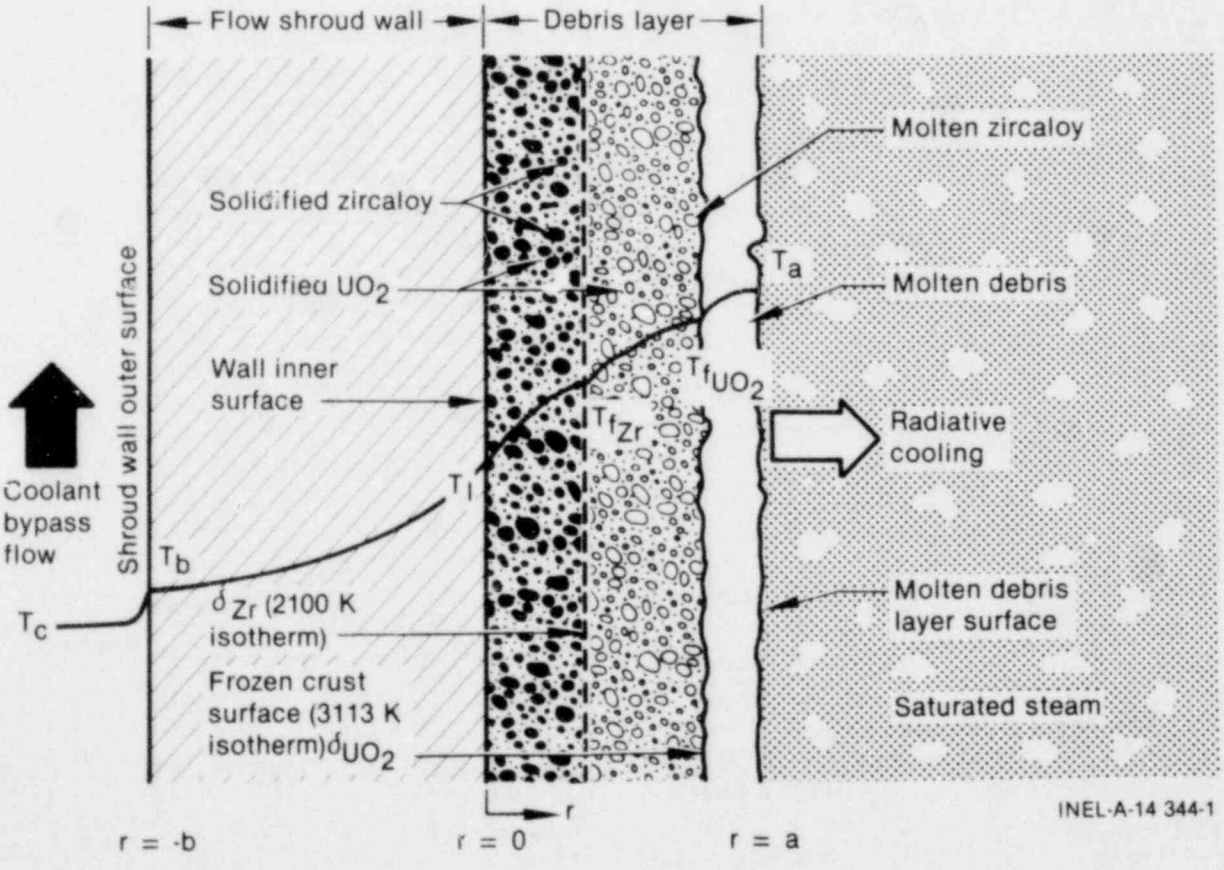

Figure 10. Physical model.

of the shroud wall, $T_I(t)$, reach a value in excess of the melting point of the wall (2100 K) upon contact with the molten debris, then freezing of the debris and simultaneous melting of the wall would occur. Otherwise, only molten debris freezing commences without melting of the wall.

In the present analysis, the axial heat conduction in the frozen crust and in the wall is neglected because of their small thicknesses with respect to their axial extents. The heat generation due to delayed fissions (that is, after the end of the power burst), and that produced by the oxidation reactions of the debris are neglected. However, the fission heating within the plated debris layer during the burst (that is, from the time of rod failure until the end of the power burst) is accounted for through the use of a rate law of the form

$$Q(t) = \nu Q_o \exp(-t/B) \quad (1)$$

where Q(t) is the fission heating rate in W/g UO_2, Q_o is the fission heating rate at the time of fuel rod failure, and B is the time constant that governs the fission heating decay rate (s^{-1}). In Equation (1), ν is an energy deposition weight factor, which is equal to the ratio of energy deposited due to thermal fissions within the debris layer (expressed in Joules per gram UO_2 per megawatt-second of the transient core energy) to the energy deposited in the cylindrical test fuel rod before failure. This weight factor is expected to be greater than unity because the neutron self-shielding in the debris layer is smaller than it is in the fuel rod due to the plated configuration and the relatively small thickness of the debris layer.

3.2 Analysis

According to the equilibrium pseudo phase diagram between UO_2 and oxygen-stablized alpha-zircaloy-4 [α-Zr(O)] shown in Figure 11, a eutectic and a monotectic could form upon freezing of the molten debris (a mixture of UO_2 fuel and zircaloy cladding). The eutectic mixture, which contains 5 mole % UO_2 and 95 mole % oxygen-stabilized alpha-zircaloy, freezes at about 2100 K. This freezing temperature is less than the melting temperatures of both UO_2 ($\sim$ 3113 K) and α-Zr(O) ($\sim$ 2200 K). Freezing of the debris would commence, however, at a temperature higher than 2100 K if the UO_2 concentration is reduced. It approaches the freezing temperature of α-Zr(O) ($\sim$ 2200 K) as the concentration of UO_2 in the debris goes to zero. The monotectic mixture contains 85 mole % UO_2 and 15 mole % α-Zr(O) and freezes at about 2640 K, which is less than the UO_2 melting point but higher than that of α-Zr(O). Molten debris with a UO_2 concentration in excess of 85 mole % would freeze, however, at a temperature in excess of 2640 K, depending on the concentration of the constituents.

Freezing of molten debris, which contains between 20 to 85 mole % UO_2, occurs in two successive stages. First, the UO_2-rich monotectic, with a composition of 85 mole % UO_2, partially freezes when the debris temperature drops below about 2640 K. Following that, the α-Zr(O)-rich eutectic [which contains about 95 mole % α-Zr(O)] within the UO_2-rich crust, which froze in the first stage, freezes when the temperature in the crust falls below 2100 K. As shown in Figure 11, the composition of the debris changes with temperature during the freezing process (that is, [Zr-rich liquid + UO_2-rich liquid] $\rightarrow$ [Zr-rich liquid + solid (U,Zr) O_{2-x}] $\rightarrow$ [solid α-Zr(O) + solid UO_2]). In the RIA-ST-4 experiment, the molten debris may have contained about 42 mole % UO_2(corresponding to a weight fraction of 22% zircaloy and 78% UO_2), which is the same as that in the test fuel rod.

The facts that the thermophysical properties of the (U,Zr) O_{2-x} solid solution is not reported in the literature and the freezing temperature and phase-transformation characteristics of the debris are strongly dependent on the composition, make it extremely difficult to study the transient freezing of the debris. To overcome this difficulty, it is assumed that the molten debris will freeze as a homogeneous mixture of UO_2 and zircaloy without any tendency to form solid solution(s). (The validity of this assumption will be examined through the comparison of calculation with experimental results.) Therefore, the thermophysical properties of the debris can be assessed in terms of those of the constituents. As a result, the freezing of the molten debris layer, as illustrated in Figure 10, is completed through two successive stages. In the first stage, the molten fuel freezes as the temperature in the debris falls below the UO_2 melting point (3113 K). Next, the molten zircaloy within the fuel crust (which froze in the first stage) freezes when the temperature in the crust drops below the melting point of zircaloy (2100 K). Therefore, two moving fronts with a change-of-phase are formed in the debris layer, which is shown in Figure 10. The advance front,

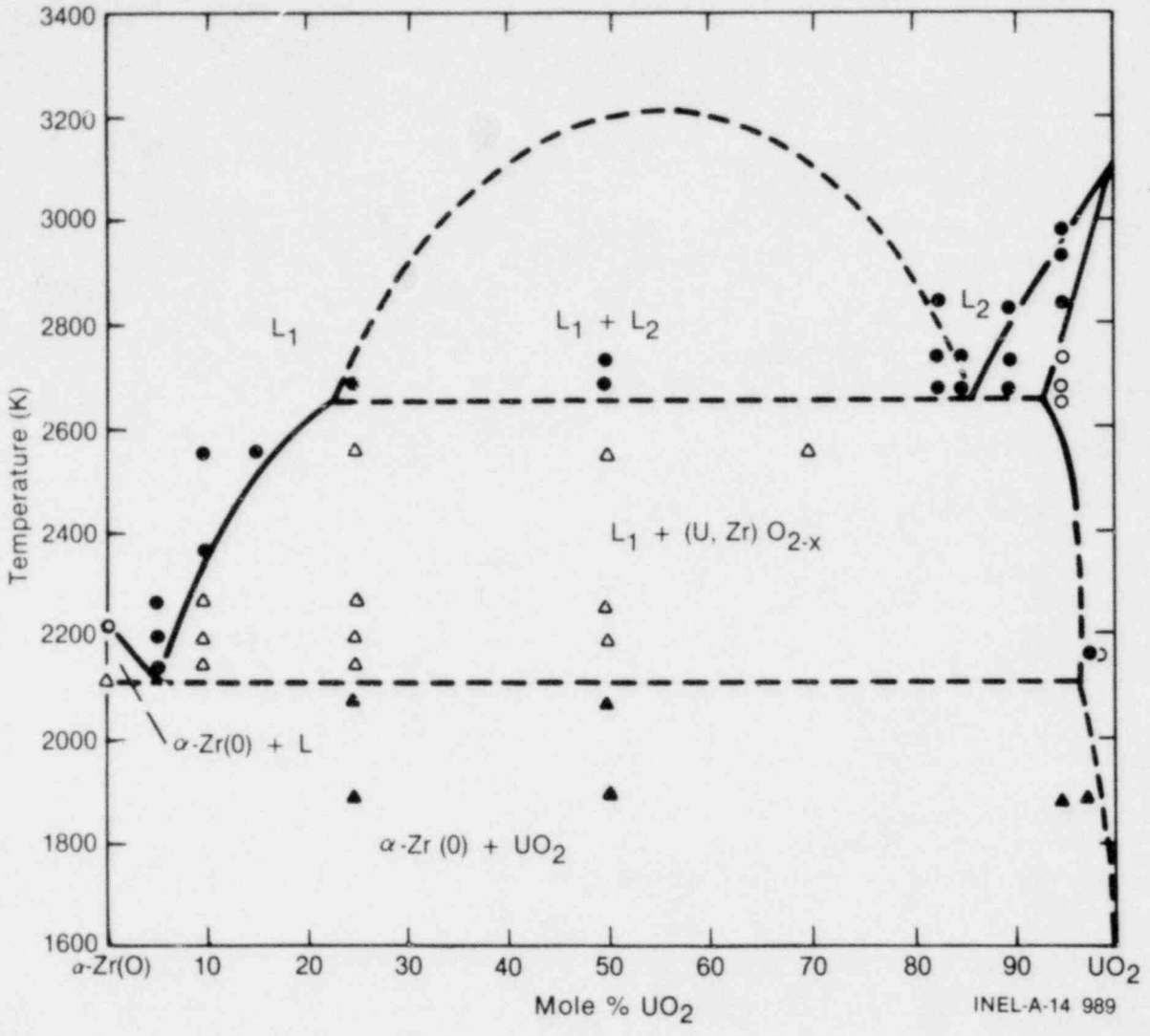

Figure 11. Equilibrium pseudo binary phase diagram between UO_2 and oxygen-stabilized α-phase zircaloy-4 [α-Zr(O)].

$r = \delta_{UO_2}$, corresponds to a temperature isotherm equal to the melting point of UO_2, and the second front, $r = \delta_{Zr}$, represents the melting point of zircaloy.

During the freezing process of the molten debris, the thermal heat is transmitted out from the debris layer, $0 \le r \le a$, by two means: the transient heat conduction through the shroud wall, and the radiative cooling at the debris layer surface, $r = a$ (to the steam generated within the test shroud upon fuel rod failure). These two mechanisms of heat transfer will strongly influence the heat transmission within the debris layer because of the small thickness of the layer. Therefore, the contribution of the internal electromagnetic radiation within the debris layer to the effective thermal conductivity of the debris can be neglected. However, in those cases in which the debris layer is thick, the effect of the internal electromagnetic radiation, far from the boundaries, could be important because of the porosity and the high melting point of the UO_2 fuel.[15-17]

3.2.1 Thermophysical Properties of the Debris. In the present analysis, the thermophysical properties of the debris and the wall are considered to be temperature dependent. The effective properties of the debris are assessed in terms of those of the UO_2 fuel and the zircaloy cladding as follows:

1. Density,

$$\rho_s = \rho_{Zr}\varepsilon + \rho_{UO_2}(1 - \varepsilon) . \qquad (2)$$

2. Heat capacity,

$$C_s = \frac{1}{\rho_s}\left[\rho_{Zr} C_{Zr} \varepsilon + \rho_{UO_2} C_{UO_2} (1 - \varepsilon)\right]. \quad (3)$$

3. Thermal conductivity[18] [see Equation (4) in box]

where the terms are as defined in the nomenclature.

3.2.2 Governing Equations

3.2.2.1 Debris Layer—The transient heat conduction equation in the debris layer ($0 \le r \le a$) is of the general form

$$\rho(T)\, C(T) \frac{\partial T}{\partial t} = \frac{1}{r}\frac{\partial}{\partial r}\left[r\, k(T) \frac{\partial T}{\partial r}\right] + \rho(T)\, Q(T) \quad (5)$$

where Q(t) is a fission heating rate defined by Equation (1), and ρ, C, and k are the effective density, heat capacity, and thermal conductivity, respectively, of the debris.

The boundary conditions at the change-of-phase fronts, $r = \delta_{Zr}$ and $r = \delta_{UO_2}$, are

$$k_s \frac{\partial T_s}{\partial r}(\delta_{Zr}, t) = k_s \frac{\partial T_s}{\partial r}[(a - \delta_{Zr}),t] + \varepsilon\, \rho_{Zr} L_{Zr} \frac{d\delta_{Zr}}{dt}, \quad (6)$$

$$T_s(\delta_{Zr}, t) = T_s[(a - \delta_{Zr}),t] = T_{f_{Zr}}, \quad (7)$$

$$k_s \frac{\partial T_s}{\partial r}(\delta_{UO_2}, t) = k_s \frac{\partial T_s}{\partial r}[(a - \delta_{UO_2}),t] + (1 - \varepsilon)\rho_{UO_2} L_{UO_2} \frac{d\delta_{UO_2}}{dt}, \quad (8)$$

and

$$T_s(\delta_{UO_2},t) = T_s[(a - UO_2),t] = T_{f_{UO_2}}. \quad (9)$$

The boundary condition at the molten debris layer surface, $r = a$, is

$$k_s \frac{\partial T_s}{\partial r}(a, t) = h_R (T_a - T_{sat}) \quad (10)$$

where T_a is the temperature at the debris layer surface, which is a function of time, and h_R is the radiative cooling coefficient at the debris layer surface. An assessment of h_R is presented in Appendix A. The initial conditions at time zero are that $\delta_{Zr} = 0$, $\delta_{UO_2} = 0$, and $T_s(r, 0) = T_D$, where T_D is the molten debris temperature at the time of fuel rod failure.

3.2.2.2 Shroud Wall—The transient heat conduction equation in the wall ($-b \le r \le 0$) is of the general form:

$$\rho(T)\, C(T) \frac{\partial T}{\partial t} = \frac{1}{r}\frac{\partial}{\partial r}\left[r\, k(T) \frac{\partial T}{\partial r}\right]. \quad (11)$$

Table 2 lists the boundary and initial conditions for cases in which melting of the wall does and does not occur. As indicated in the table, two modes of heat transfer are considered to occur at the shroud wall outer surface during the freezing process of the debris layer, namely, forced convection heat transfer and stable film boiling heat transfer. Stable film boiling is assumed to commence as soon as the temperature at the shroud

$$k_s = k_{UO_2} \frac{\left\{2 + (k_{Zr}/k_{UO_2}) - 2\varepsilon\left[1 - (k_{Zr}/k_{UO_2})\right]\right\}}{\left\{2 + (k_{Zr}/k_{UO_2}) + \varepsilon\left[1 - (k_{Zr}/k_{UO_2})\right]\right\}}. \quad (4)$$

Table 2. The boundary and initial conditions in the shroud wall ($-b \leq r \leq 0$)

Item	Without Simultaneous Melting of the Wall	With Simultaneous Melting of the Wall
		(a) In the solid-region of the wall ($-b \leq r \leq -\delta_m$)
Boundary conditions	$k_w \frac{\partial T_w}{\partial r}(0, t) = k_s \frac{\partial T_s}{\partial r}(0,t)$	$k_w \frac{\partial T_w}{\partial r}[-(b - \delta_m), t] = k_m \frac{\partial T_m}{\partial r}(-\delta_m, t) - \rho_w L_m \frac{d\delta_m}{dt}$
	$k_w \frac{\partial T_w}{\partial r}(-b, t) = h_c (T_b - T_c)$, if $T_b < T_{crit}$	The same
	$k_w \frac{\partial T_w}{\partial r}(-b, t) = h_B (T_b - T_c)$, if $T_b \geq T_{crit}$	The same
	$T_w (0, t) = T_l (t)$	$T_w (-\delta_m, t) = T_{mp}$.
		(b) In the wall molten layer ($-\delta_m \leq r \leq 0$)
		$k_m \frac{\partial T_m}{\partial r}(0, t) = k_s \frac{\partial T_s}{\partial r}(0, t)$,
		$T_m (-\delta_m, t) = T_{mp}$,
		$T_m (0, t) = T_l (t)$.
Initial conditions	$T_w (-r, 0) = T_c$.	The same
		$\delta_m (t = 0) = 0$.

wall outer surface reaches or exceeds the critical temperature of the coolant (T_{crit}). The forced convection heat transfer coefficient, h_c, and the stable film boiling heat transfer coefficient, h_B, at the wall outer surface are evaluated in Appendix B.

3.3 Method of Solution

An approximate numerical solution to the physical model shown in Figure 10 is obtained by solving the governing equations using a one-dimensional, finite element computer code, SINGLE. The boundary and initial conditions were those listed in the previous section [Equations (2) through (11) and Table 2]. The SINGLE code handles steady state and transient heat transfer problems, with or without a change-of-phase, in a plane, cylindrical, or a spherical geometry. Several options are allowed in the code; they are (a) constant or temperature-dependent thermophysical properties, (b) constant or time-dependent internal heat generation, and (c) different boundary conditions of the first (constant temperature), second (heat flux), third (radiation), or fourth (conduction or convection) kind, all of which may vary with time.

The numerical solution in SINGLE is formulated using a finite element technique based on the method of weighted residuals (MWR).[19] This method is a technique for obtaining approximate solutions for linear or nonlinear partial differential equations. The weighted residuals method seeks a solution close to the exact solution so as to approximately satisfy the given governing equations and boundary conditions. The difference between the approximate and the exact solution (residual) is required to vanish over the entire solution domain. The property of solution continuity is then invoked to maintain a small error over the whole integration field. The accuracy of the SINGLE code in solving transient heat conduction problems with phase changes is assessed in Appendix C. The predictions of the code are within 2 to 9% of the exact solutions for the solidification of a stagnant, superheated liquid on an isothermal and on a semi-infinite cold wall that melts simultaneously.

3.4 Results and Discussion

This section presents, in order, a discussion of the effects of internal heat generation in the debris, molten debris temperature and radiative cooling at the debris layer surface, zircaloy volume ratio within the debris, and initial temperature of the shroud wall on the freezing process of the debris layer and the potential erosion of the wall due to melting. Calculated are the instantaneous values of the functions, namely, the frozen crust thickness, $\delta_{UO_2}(t)$; the moving change-of-phase front, $\delta_{Zr}(t)$; the temperature at the molten debris layer surface, $T_a(t)$; the temperature of the shroud wall inner surface, $T_i(t)$; and the temperature of the wall outer surface, $T_b(t)$. If wall melting is to commence at the wall inner surface upon contact by the molten debris, the instantaneous thickness of the wall molten layer, $\delta_m(t)$, is calculated in addition to the other time-dependent functions (that is, δ_{UO_2}, δ_{Zr}, T_a, T_I, and T_b).

The parameters for a reference case are listed in Table 3, and the results of the calculations are plotted in Figure 12. Figure 12 presents a plot of the frozen crust thickness (in a percentage of the initial thickness of the molten debris layer) versus time in milliseconds. The zero mark on the ordinate represents the inner surface of the shroud

Table 3. Parameters for a reference case

Initial molten debris temperature (K)	3500
Zircaloy volume ratio within the debris	0.13
Wall thickness (mm)	3.05
Coolant bypass flow temperature (K)	538
Fission heating rate within the debris at time of rod failure, Q_o (W/g UO_2)	$\sim 8 \times 10^4$
Fission heating time constant, B, (s^{-1})	110
Energy deposition weight factor, ν	Unity

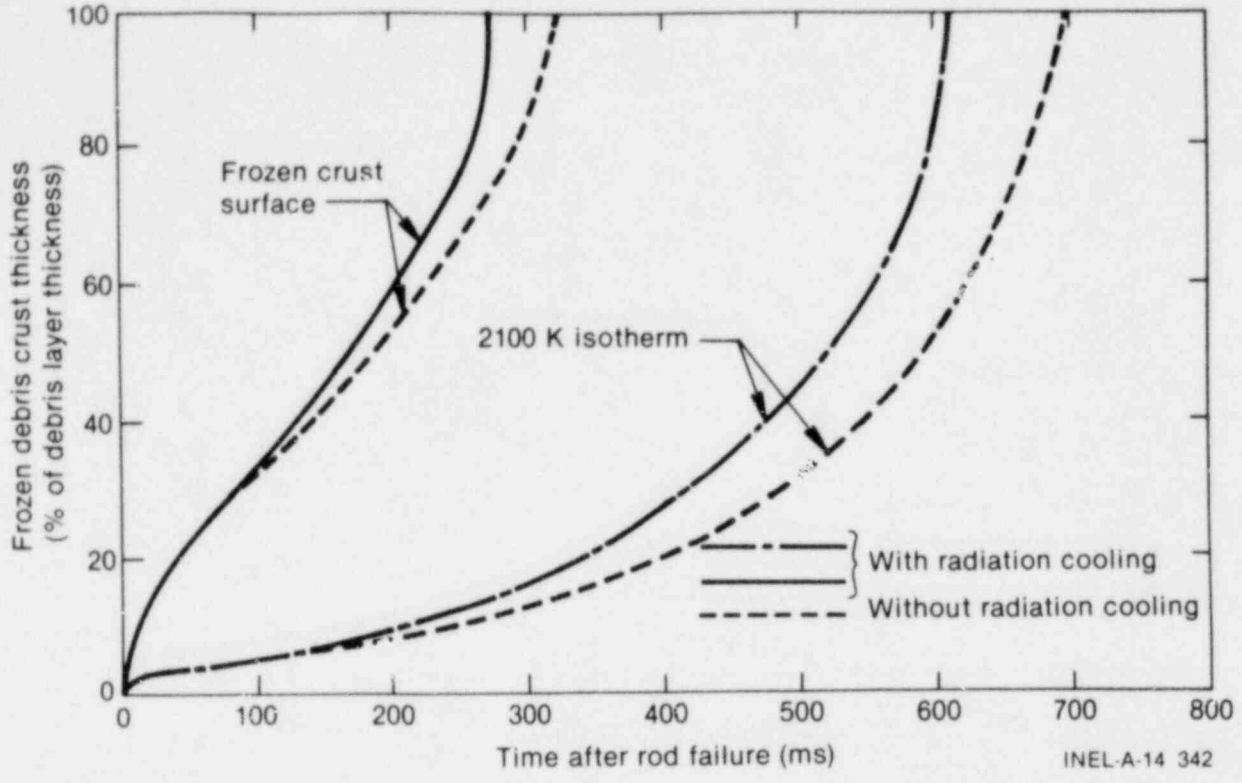

Figure 12. Transient freezing of the molten debris layer on the inner surface of the test shroud wall (reference case).

wall and the hundred mark corresponds to the molten debris layer surface. This surface, r = a, is being cooled by thermal radiation to the water vapor present within the shroud. At the time of initial contact (time zero), the transient heat conduction through the shroud wall, which is finite in thickness, caused the temperature of the wall inner surface, T_I, to reach a value which is less than the melting point of the wall material (see Subsection 3.4.5), indicating that wall melting is impossible with the conditions listed in Table 3.

The solidification front, δ_{UO_2}, corresponding to the melting point of UO_2 (3113 K, represented by the solid line in Figure 12), appears at the wall inner surface, r = 0, moving into the molten debris layer, away from wall. Following that, the molten zircaloy in the solidified UO_2 crust freezes when the temperature within the crust drops below the melting point of zircaloy (2100 K). The change-of-phase front corresponding to the melting point of the zircaloy, δ_{Zr}, is presented in Figure 12 by a broken line. As indicated, the radiative cooling at the molten debris layer surface has influenced the freezing of the debris by cooling it down and thus reducing the total freezing time. In Figure 12, the total freezing time of the UO_2 crust is reduced from 320 to 275 ms because of the radiative cooling at the debris layer surface.

Figure 13 presents the transient temperature distribution in the wall and in the debris layer at different times during the freezing process. As indicated, the debris temperature increases initially with time because of the internal heat generation. After that, however, the debris temperature declines continuously with time, since no more heat is generated in the debris after the end of the power burst (that is, approximately 45 ms after the time of contact). (The effect of internal heat generation on the temperature at the debris layer surface, T_a, is discussed in the next subsection.) On the other hand, the temperature in the wall increases with time, as demonstrated in Figure 13. A thermal front diffuses through the wall, far from the wall inner surface, until it reaches the wall outer surface, r = -b, causing the wall surface temperature, T_b, to change with time. This thermal front reaches the wall outer surface after a time ($\sim$ 76 ms) equal to the thermal response time of the wall, which is $\simeq b^2/16\alpha_w$.

3.4.1 Effects of Internal Heat Generation. The effect of internal heat generation in the debris

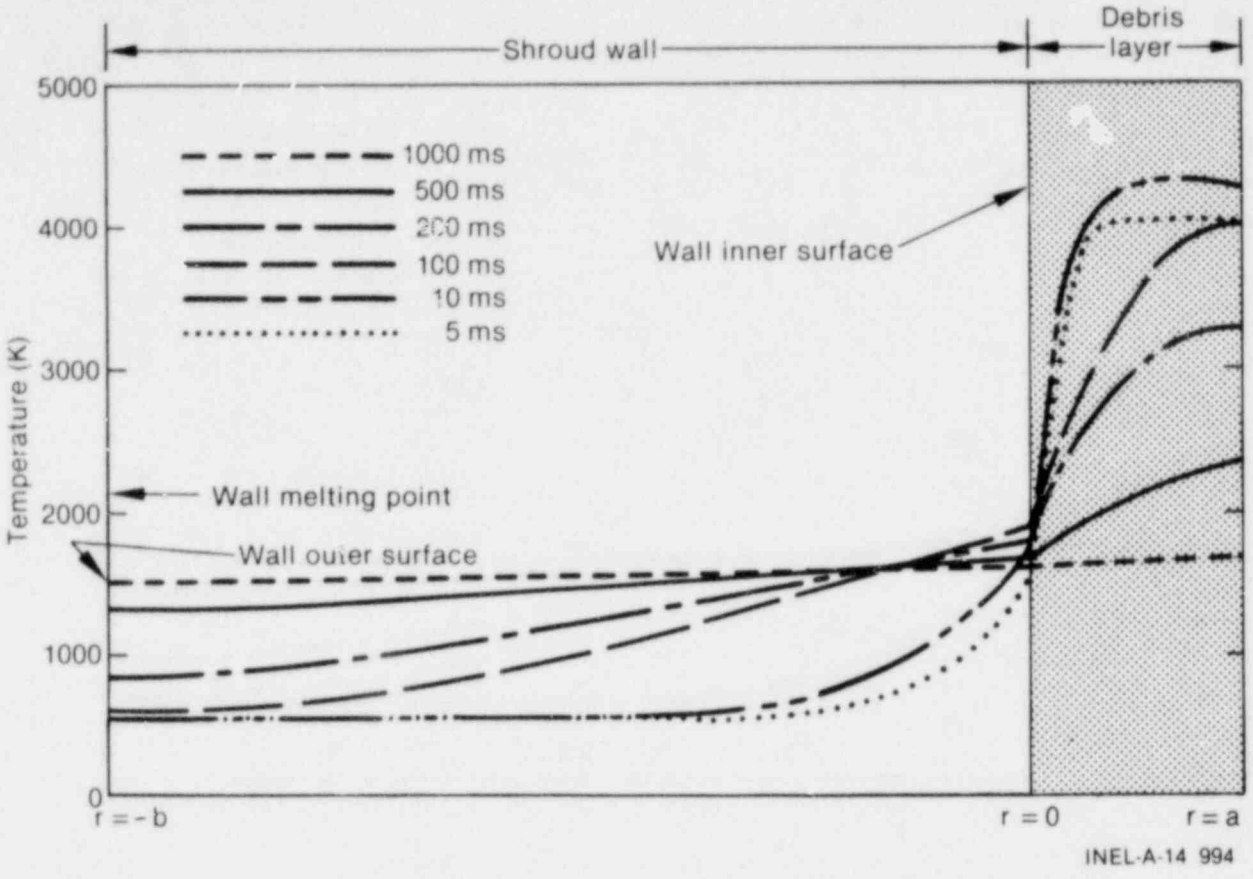

Figure 13. Transient temperature distribution in the debris layer and in the wall (reference case).

layer (from the time of rod failure until the end of the power burst) on the transient freezing of the debris is assessed in Figure 14 in terms of an energy deposition weight factor ν. In Figure 14, $\nu = 0$ represents the case without fission heating in the debris, and $\nu = 1$ represents the case in which the fission heating rate, Q(t), is of the same magnitude as in the test fuel rod before failure. Practically, the energy deposition in the debris layer is expected to be higher than unity (that is, $\nu > 1$) because of the plated configuration and the small thickness of the debris layer. This latter case is presented in Figure 14 by $\nu = 1.2$ and 1.5, respectively. As indicated, increasing the fission heat rate in the debris (that is, increasing ν) slows down the freezing of the debris and increases the total freezing time of the debris layer. This is expected, since increasing the internal heat generation increases the deposited thermal energy within the debris layer, thus increasing the effective cooling time of the debris. However, note that neglecting the fission heating of the debris, ($\nu = 0$) would result in a substantial error in assessing the transient freezing of the debris and its total freezing time. As shown, decreasing ν from unity to zero results in almost a twofold reduction of the freezing time of the debris layer (from 270 to 150 ms).

Figure 15 demonstrates the effects of the internal heat generation on the temperature at the debris layer surface, $T_a(t)$. For $\nu \geq 1$, T_a increases initially with time until it reaches a peak value, at which time the rate of energy deposition balances that which can be conducted away through the wall and transferred out by radiation at the surface of the debris layer. After that time, however, the internal heat generation within the debris becomes negligibly small, and thus the temperature, $T_a(t)$, declines with time. Note that increasing ν from unity to 1.2 increases the peak temperature at the debris layer surface from 4470 to 4700 K.

3.4.2 Effects of Molten Debris Temperature and Radiative Cooling. Figure 16 demonstrates the effects of the initial molten debris temperature, T_D, and the radiative cooling at the debris layer surface on the freezing process of the debris layer. As shown, increasing the molten

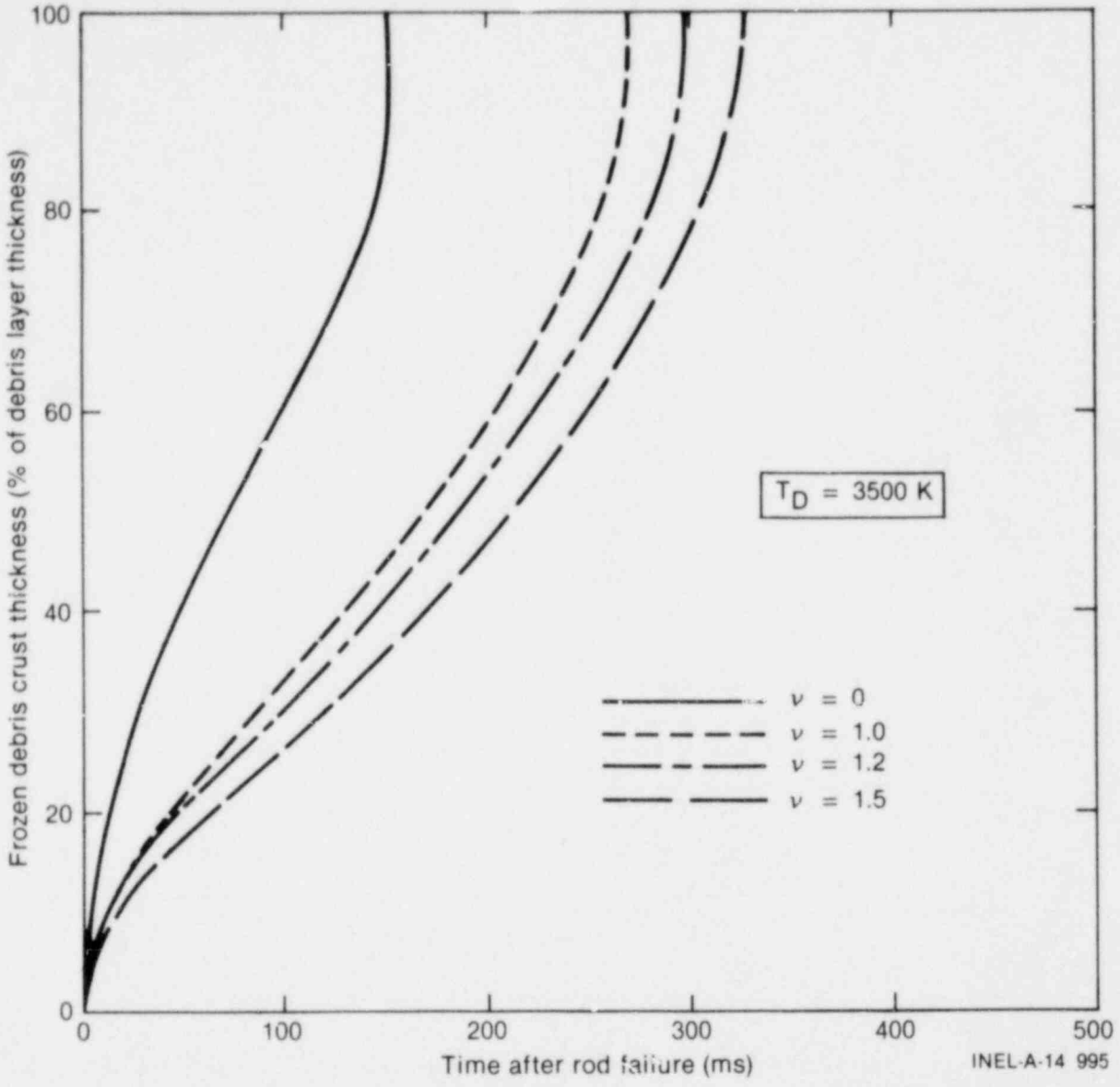

Figure 14. Effect of internal heat generation on the transient freezing of the molten debris layer.

debris temperature or neglecting the radiative cooling slows down the freezing process and increases the total freezing time of the debris layer. For example, increasing the initial debris temperature from 3150 to 5000 K results in an almost twofold increase in the total freezing time. Neglecting the effect of the radiation cooling, however, would overestimate the total freezing time by only about 25%.

3.4.3 Oxidation of the Shroud Wall Outer Surface. The temperature-time history at the shroud wall inner and outer surfaces during the freezing process of the debris layer depends on the initial debris temperature and the internal heat generation in the debris. This is illustrated in Figures 17 and 18 which present the temperature-time histories at the wall inner and outer surfaces, respectively, as functions of the debris temperature and the internal heat generation in the debris. In those figures, time zero is the time at which the inner surface of the wall was contacted by the molten debris upon rod failure.

As shown in Figure 18, film boiling commences at the shroud wall outer surface shortly after the time of contact with the debris, causing rapid wall overheating and oxidation of the wall outer sur-

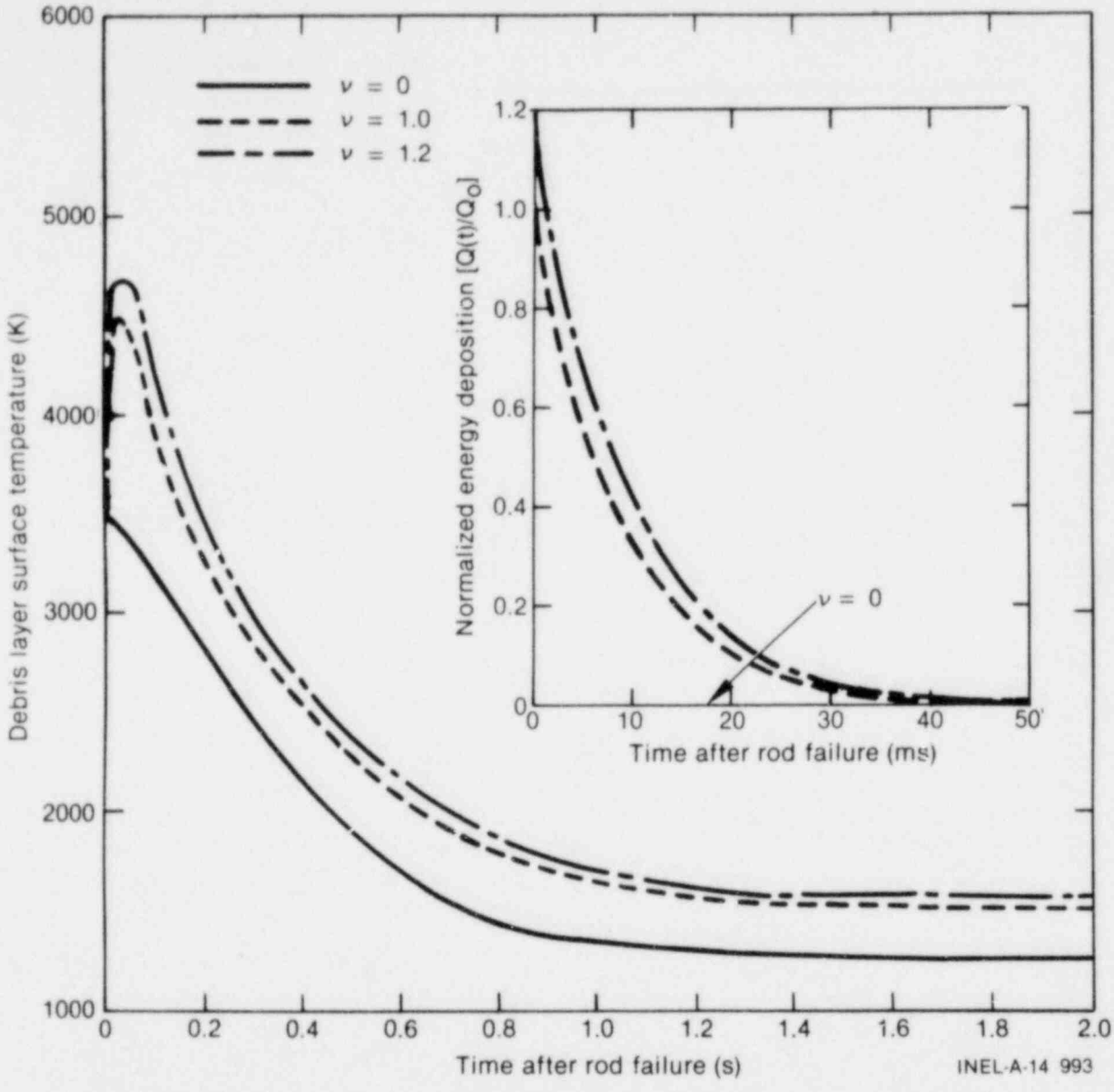

Figure 15. Effect of internal heat generation on the temperature at the debris layer surface.

face due to the steam-zircaloy reaction during film boiling. The peak temperature at the wall outer surface and the duration of film boiling are increased as the molten debris temperature or the internal heat generation in the debris are increased. For example, increasing the debris temperature from 3500 to 4000 K increases the wall surface peak temperature from 1520 to 1710 K, with a slight increase in the duration of film boiling.

Because the shroud wall is made of zircaloy-4 and the oxidation kinetics of zircaloy by water vapor are well-known functions of temperature and time,[11,12] the thicknesses of the ZrO_2 and oxygen-stabilized alpha-zircaloy layers formed on the wall outer surface during film boiling can be calculated and compared with the measured thicknesses of those layers.

The oxidation of the shroud wall outer surface during film boiling is assessed using the temperature-time history presented in Figure 18. The transient thicknesses of the ZrO_2 and alpha-zircaloy layers are calculated through the use of the following correlations:[11]

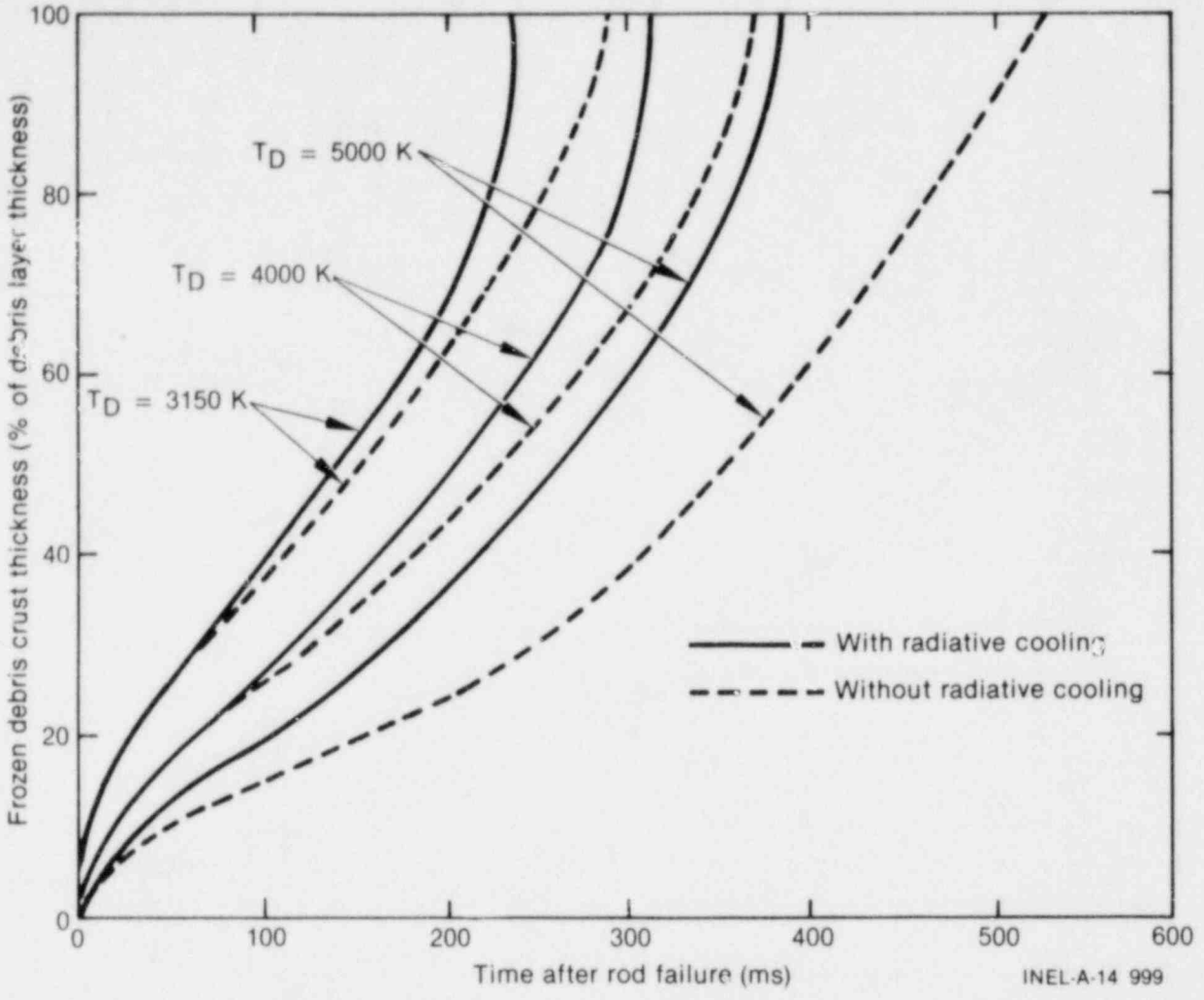

Figure 16. Effect of molten debris temperature and radiative cooling on the transient freezing of the debris layer.

$$\delta_{ZrO_2}(t) = \left\{ 0.02252\ t \begin{pmatrix} +29\% \\ -22\% \end{pmatrix} \right.$$
$$\left. \text{EXP}\ [-35890\ (\pm 2.1\%)/RT] \right\}^{1/2} \qquad (12a)$$

$$\delta_{\alpha\text{-}Zr}(t) = \left\{ 1.5230\ t \begin{pmatrix} +54\% \\ -35\% \end{pmatrix} \right.$$
$$\left. \text{EXP}\ [-48140\ (\pm 2.6\%)/RT] \right\}^{1/2} \qquad (12b)$$

where δ_{ZrO_2} and $\delta_{\alpha\text{-}Zr}$ are the thicknesses of the ZrO_2 and alpha-zircaloy oxide layers, respectively; T is the wall surface temperature in Kelvin; t is the time in seconds; and R is the universal gas constant.

The instantaneous thicknesses of the oxide and alpha-zircaloy layers are plotted in Figure 19 for two different molten debris temperatures, 3150 and 3500 K. As shown, the oxide and α-Zr(O) layers thicken with time until the wall surface temperature drops below about 1100 K. Increasing the molten debris temperature increases the wall peak temperature, thus increasing the thicknesses of the ZrO_2 and α-Zr(O) layers.

The calculated oxide thicknesses, as functions of the total fuel enthalpy, I, at the time of rod failure and the internal heat generation in the debris, are compared with the measured thicknesses in Figure 20. The dark horizontal areas in the figures represent the uncertainty in the measured thicknesses, and the solid lines represent

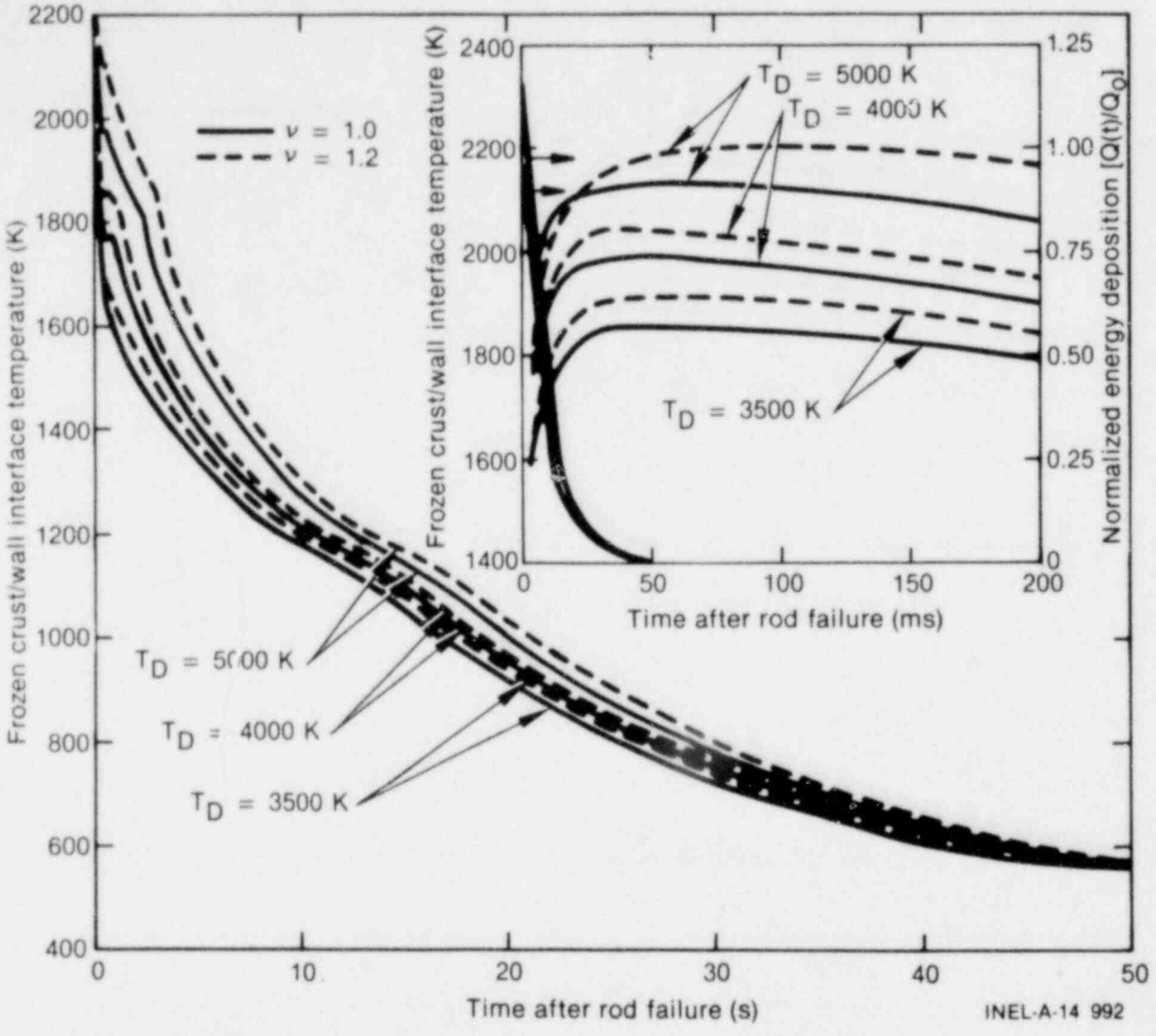

Figure 17. Temperature-time history at the shroud wall inner surface.

the calculated thicknesses. The fuel enthalpy at the time of rod failure is calculated through use of the following equation:

$$I = \int_0^{T_f} C_{sf}(T)dT + L_f + \int_{T_f}^{T_d} C_{mf}(T)dT. \quad (13)$$

The expression for the solid fuel heat capacity $C_{sf}(T)$, is given in Reference 20 as a function of temperature. For molten UO_2, however, the heat capacity, C_{mf}, is taken to be constant and equal to 500 J/kg·K.

It is concluded from Figure 20 that the total fuel enthalpy at the time of fuel rod failure was in the range of 1400 to 1520 J/g UO_2, which corresponds to an initial debris temperature of about 3240 to 3500 K. These values of fuel enthalpy are in agreement with the total fuel enthalpy calculated from the energy deposition during the burst (≈1465 J/g UO_2). The figure also indicates that the energy deposition in the molten debris layer, expressed in Joules per gram UO_2 per megawatt-second of the transient core energy, was no more than 20% higher than that in the test fuel rod before failure (that is, $1.0 \leq \nu \leq 1.2$).

3.4.4 Effect of Zircaloy Volume Ratio Within the Debris. The transient freezing of the molten debris layer is influenced by the zircaloy volume

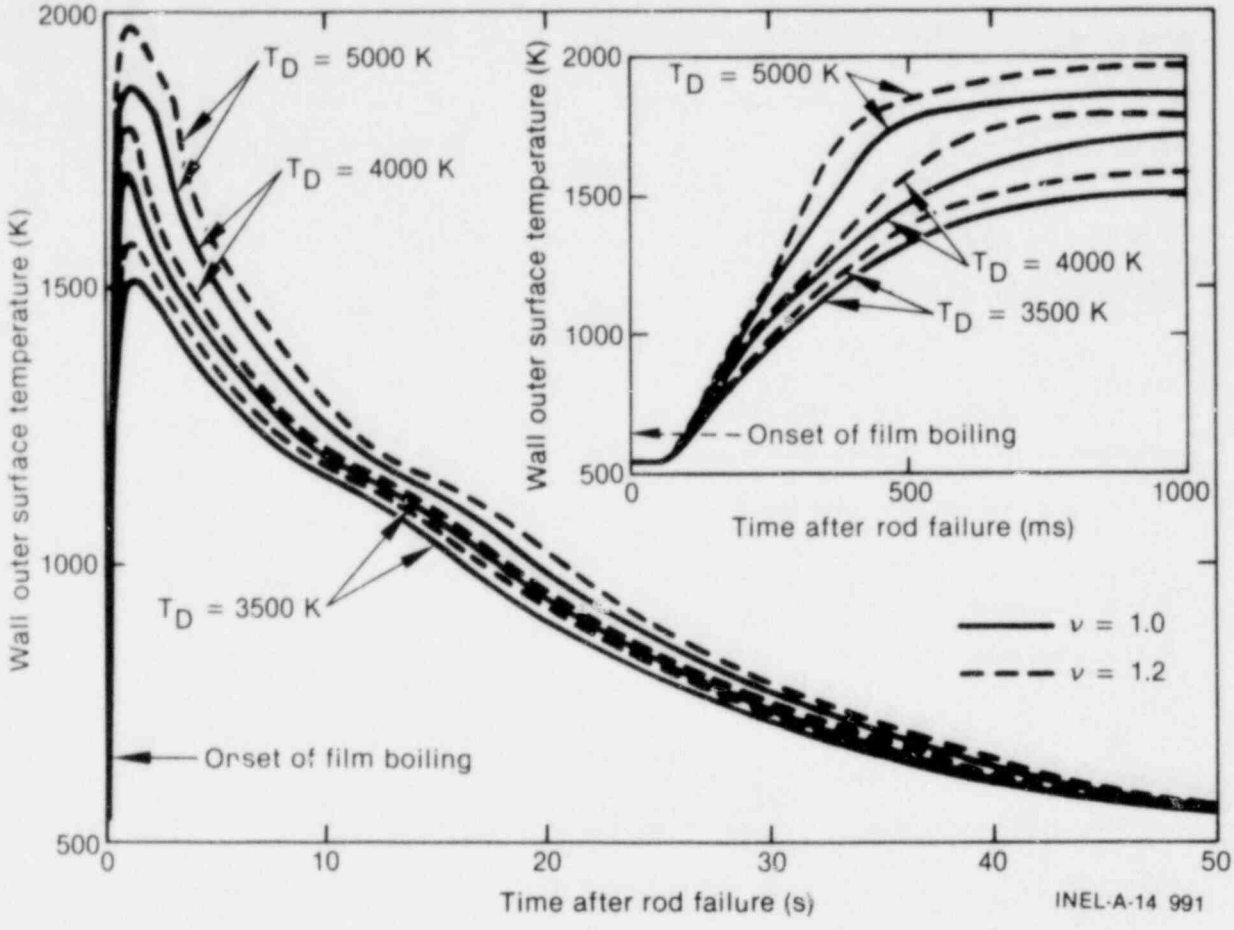

Figure 18. Temperature-time history at the shroud wall outer surface.

ratio in the debris. This follows from the fact that the zircaloy thermal properties are higher than those of the UO_2 fuel, that is $(\rho_{Zr}\ C_{Zr}\ k_{Zr}) > (\rho_{UO_2}\ C_{UO_2}\ k_{UO_2})$. Therefore, increasing the zircaloy ratio increases the effective thermal conductivity of the debris, thus accelerating the freezing process. Figure 21 illustrates the effect of the zircaloy volume ratio on the total freezing time of the molten debris layer. As indicated, a fourfold increase in the zircaloy volume ratio (from 10 to 40%), reduces the total freezing time by approximately 50%.

As pointed out in the previous section, melting of the shroud wall inner surface upon being contacted by the molten debris did not occur during the RIA-ST-4 experiment. The conditions under which erosion of the wall due to melting can occur are assessed in the following subsection.

3.4.5 Potential for Erosion of the Shroud Wall Due to Melting. Figure 22 illustrates the effects of the internal heating in the debris and the initial wall and molten debris temperatures on the maximum temperature obtainable at the inner surface of the wall upon contact by the molten debris. As indicated, partial melting of the wall would occur if the wall temperature was initially higher than 1000 K and the molten debris temperature was in excess of about 3500 K. Under such conditions, the temperature of the wall inner surface reaches a value which is higher than the melting point of the wall materials (2100 K) and less than the freezing temperature of the fuel (3113 K), resulting in wall melting and simultaneous freezing of the molten debris layer. As shown in Figure 22, increasing the fission heating in the debris (that is, increasing) reduces the threshold temperatures of the wall and of the molten debris at which wall melting commences.

Figure 23 depicts the transient growth (melting) and decay (freezing) behavior of the wall molten layer when the initial wall temperature is equal to 1500 K. When the molten debris temperature is higher than 5000 K, complete melting of the wall

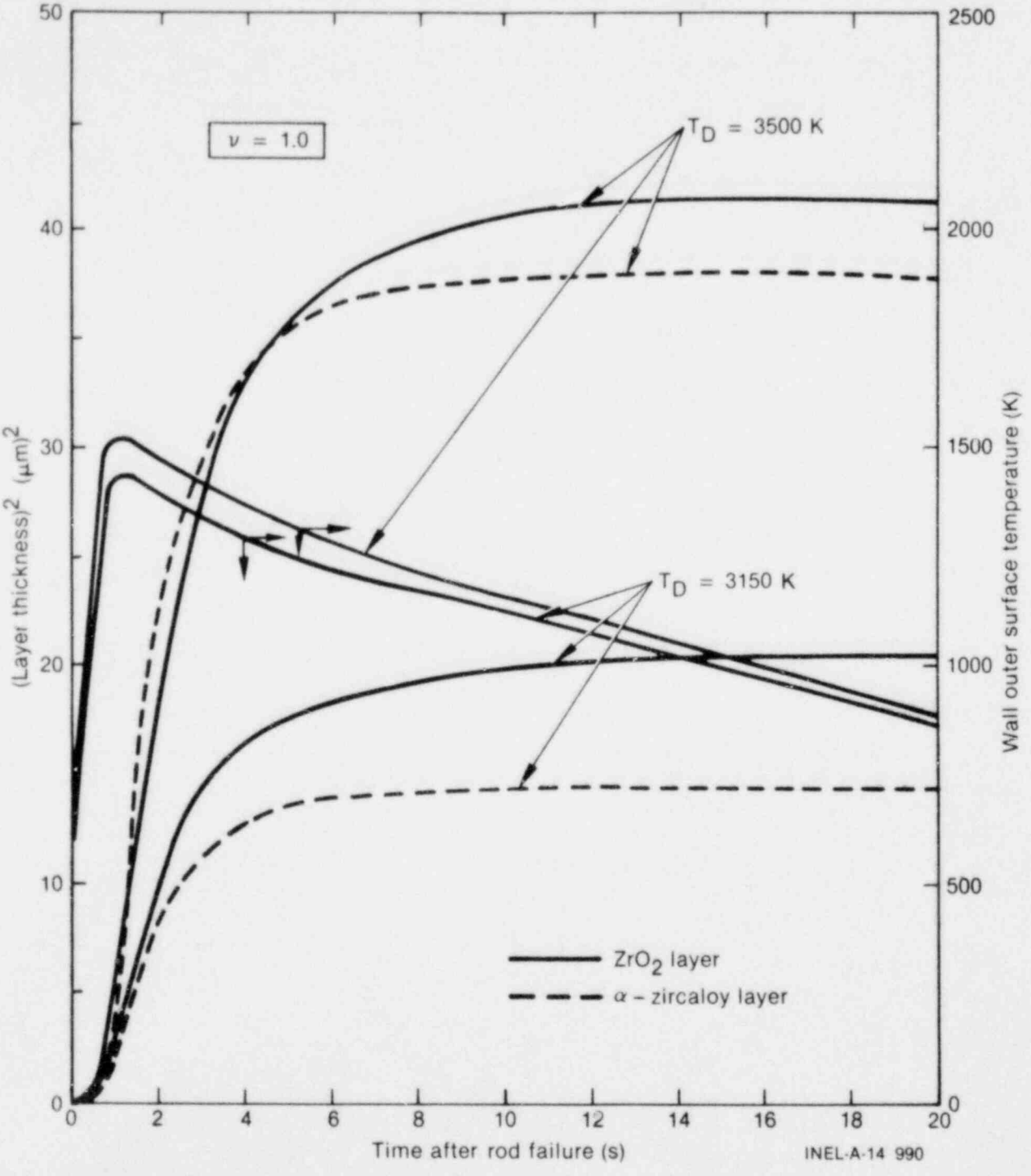

Figure 19. Transient growth of the oxide layers on the shroud wall outer surface.

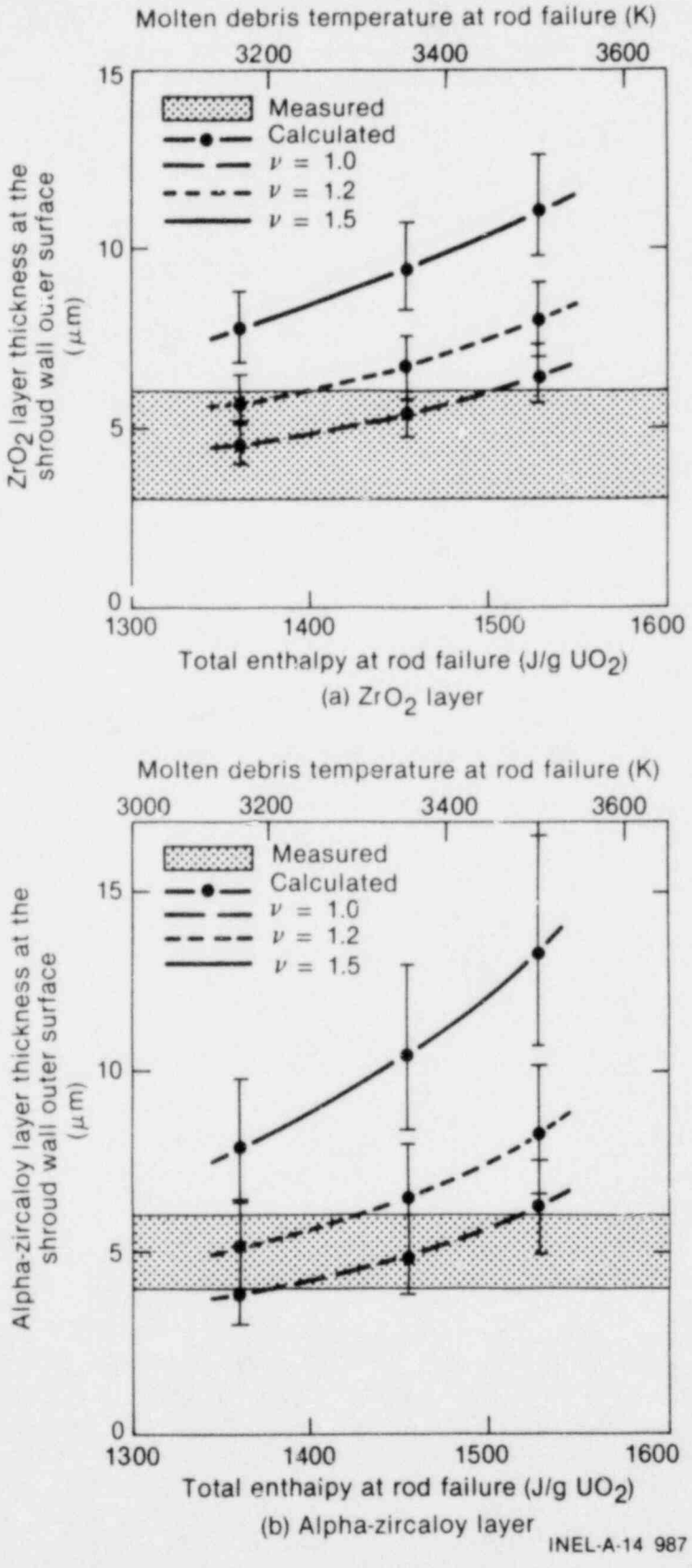

Figure 20. Comparison between calculated and measured oxide layer thicknesses on the shroud wall outer surface.

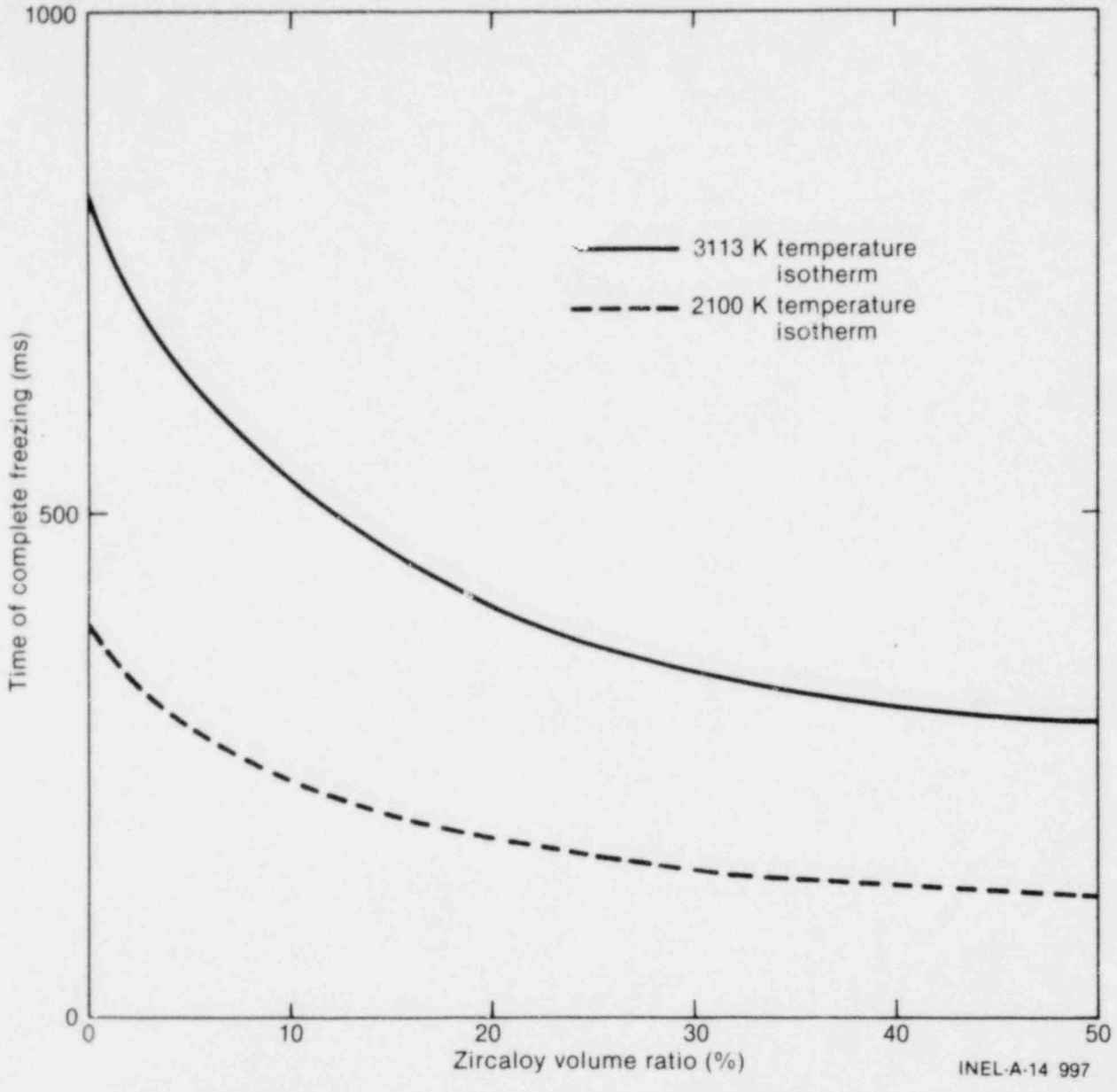

Figure 21. Effect of zircaloy volume ratio on total freezing time of the debris layer.

occurs after approximately one second. With the debris temperatures less than or equal to 4000 K, however, the melting process of the wall is unstable because of the small thickness of the wall and the continuous cooling at its outer surface.[7] The molten layer within the wall thickens with time until it reaches a maximum thickness (less than the initial thickness of the wall) when the conductive heat flux from the frozen debris crust to the wall balances that which can be conducted away through the unmelted region of the wall. Then, the wall molten layer thins by freezing and eventually disappears. During the freezing process of the wall molten layer, the heat flux conducted through the unmelted region of the wall to the coolant becomes higher than the conductive heat flux from the frozen debris crust to the wall. As evidenced in Figure 23, increasing the molten debris temperature increases the conductive heat flux to the wall, and thus increases the maximum melting of the wall and the total lifetime of the wall molten layer. For instance, increasing the molten debris temperature from 3500 to 4000 K increases the maximum thickness of the wall

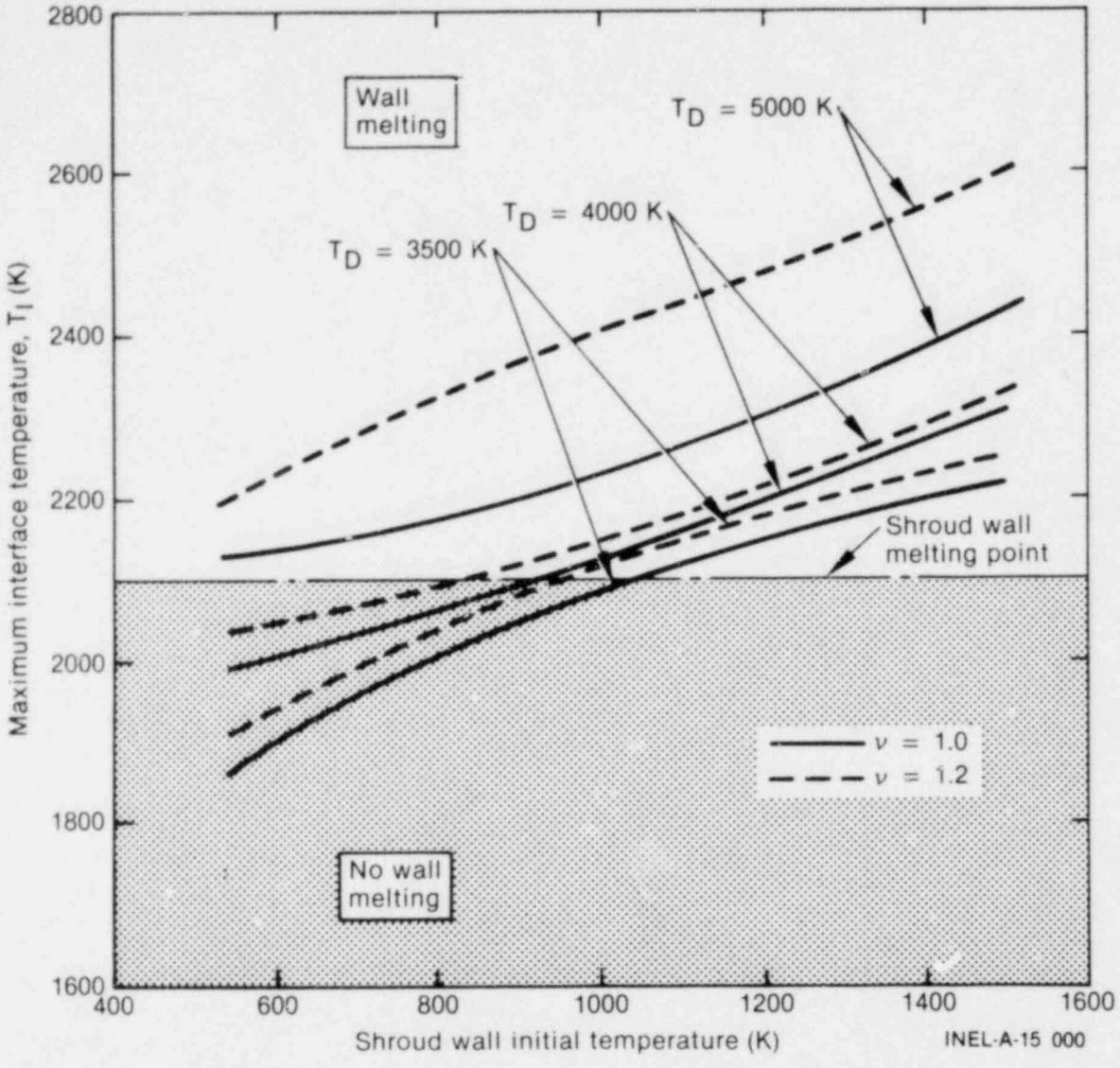

Figure 22. Effects of initial wall and molten debris temperatures on the temperature at the wall inner surface.

molten layer from 37 to 65% of the initial thickness of the wall, and increases its total lifetime from 2.7 to 4.1 s.

Note that radiative cooling at the debris layer surface, r = a, strongly influences the transient melting of the wall. The effect of radiative cooling on the growth and decay behavior of the wall molten layer is demonstrated in Figure 23 by the broken lines. As shown, the radiative cooling of the debris slows down the melting process of the wall, reduces the maximum wall melting, and decreases the total lifetime of the wall molten layer. This is expected, since thermal radiation at the debris layer surface cools down the debris and decreases the amount of heat available to cause further melting of the wall.

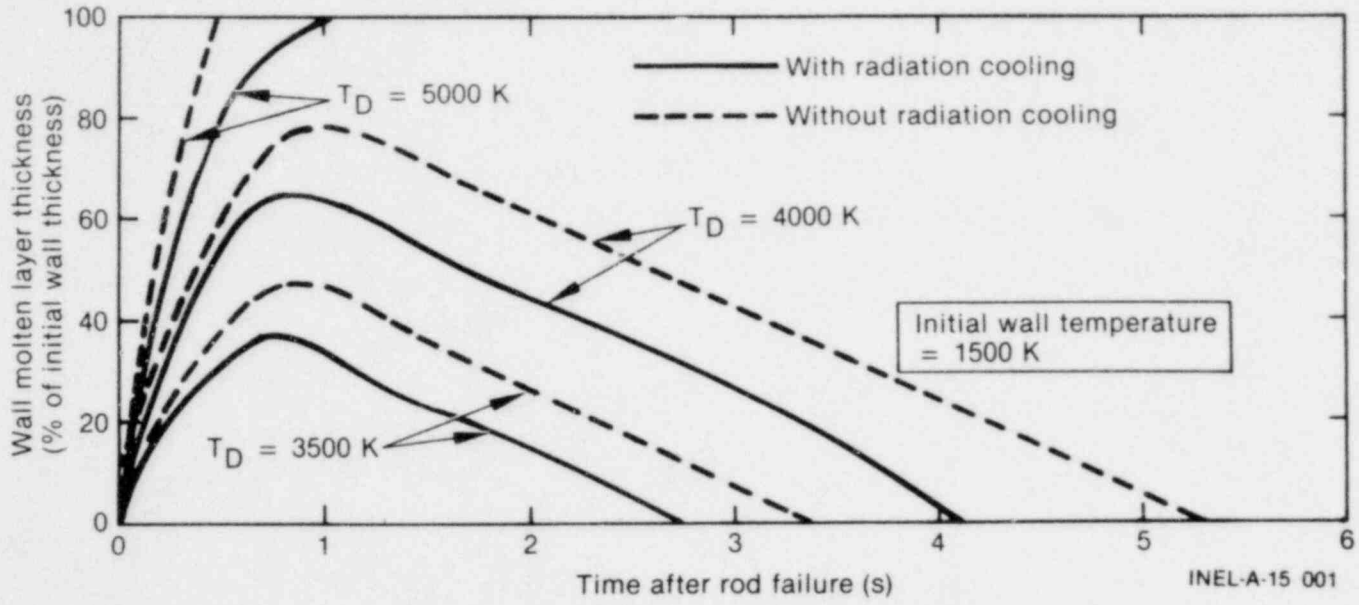

Figure 23. Transient growth and decay behavior of the wall molten layer.

4. CONCLUSIONS

The transient freezing of a molten debris layer (primarily a mixture of UO_2 and zircaloy) deposited on the inner surface of the RIA-ST-4 shroud wall has been analyzed, and the potential for wall melting upon contact with molten debris has been assessed. Analysis of this two-component, simultaneous freezing and melting problem in a finite medium was performed using a one-dimensional, finite element computer code, SINGLE, based on the method of weighted residuals. The code was found to be accurate to within 2% of the exact solution for the transient freezing of a stagnant, superheated liquid on an isothermal wall, and to within 9% for the freezing on a semi-infinite wall that melts simultaneously.

The analysis indicated that transient freezing of the molten debris layer was governed by transient heat conduction through the shroud wall and radiative cooling at the debris layer surface. The initial debris temperature, the internal heat generation in the debris, the zircaloy volume ratio within the debris, and the initial wall temperature strongly influenced the debris freezing process and the potential for wall melting. Increasing the molten debris temperature or the internal heat generation in the debris, or both, increases the total time required for freezing of the debris layer. Analysis showed that increasing the zircaloy volume ratio within the debris increases the effective thermal conductivity and thus reduces the total freezing time of the molten debris layer.

The comparison of the calculated oxide layer thicknesses (ZrO_2 and alpha-zircaloy layers), which were formed at the shroud wall outer surface due to the steam-zircaloy reaction during film boiling, with the measured thicknesses indicated that (a) the total enthalpy at the time of rod failure was about 1460 $\pm$ 60 J/g UO_2, which is in excellent agreement with the fuel enthalpy calculated from the energy deposition during the power burst ($\sim$1465 J/g UO_2), and (b) the rate of energy deposition in the plated debris layer was no more than 20% higher than that in the rod before failure. Such an increase in energy deposition rate is expected because the neutron self-shielding in the debris layer is smaller than it is in the fuel rod.

The potential for melting of the wall depends on the radiative cooling at the debris layer surface, the internal heat generation within the debris, and the temperatures of the wall and of the molten debris at the time of contact. The radiative cooling at the debris layer surface slows down the melting process of the wall; it reduces the maximum melting of the wall and the total lifetime of the wall molten layer. Therefore, the analysis of transient debris freezing on cold core structures following a hypothetical core meltdown accident in LWRs should consider the effect of thermal radiation in cooling the debris during the freezing process, rather than transient conduction through walls.

It was concluded from the calculations that the RIA-ST-4 shroud wall should not melt upon contact with molten debris, which agrees with the experimental observations, because of the initial low temperatures of the wall (538 K) and of the molten debris (3500 K) at the time of contact (test fuel rod failure time). Melting of the shroud wall would occur if the initial wall temperature was higher than 1000 K and the molten debris temperature was in excess of 3500 K. However, because of the small thickness of the wall and the continuous cooling at the wall outer surface by coolant bypass flow, the wall molten layer is unstable. It would thicken until it reached a maximum thickness less than the initial thickness of the wall, and then thin by freezing and ultimately disappear.

The present study indicates that treating the molten debris during the transient freezing process as a homogeneous mixture of UO_2 and zircaloy, in which the effective thermophysical properties of the debris are assessed in terms of those of the constituents, is a reasonable assumption. The agreement between the calculations and the experimental results strongly support the validity of the physical model, the simplifying assumptions, and the analytical approach presented in the current work. This analysis could be applied with minimum modifications to assess the freezing of molten core debris on cold core structures following a hypothetical core meltdown accident in light water reactors.

5. REFERENCES

1. C. Zimmermann et al., *Experiment Data Report for Test RIA-ST (Reactivity Initiated Accident Test Series)*, NUREG/CR-0473, TREE 1235, March 1979.

2. R. S. Semken et al., *Reactivity Initiated Accident Test Series, RIA Scoping Test Fuel Behavior Report*, NUREG/CR-1360, EGG-2024, April 1980.

3. H. S. Carslaw and J. C. Jaeger, *Conduction of Heat in Solids*, 2nd edition, Oxford: Clarendon Press, 1959.

4. P. M. Heertjes and Ir Ong Tjing Gie, "Crystallization of Water by Unidirectional Cooling," *British Chemical Engineering, 5*, 6, 1960, pp. 413-419.

5. M. S. El-Genk and A. W. Cronenberg, "Solidification in a Semi-Infinite Region with Boundary Conditions of the Second Kind: An Exact Solution," *Letters in Heat and Mass Transfer, 6*, 1979, pp. 321-327.

6. M. Epstein, "Heat Conduction in the UO_2-Cladding Composite Body with Simultaneous Solidification and Melting," *Nuclear Science and Engineering, 51*, 1973, pp. 84-87.

7. M. S. El-Genk and R. L. Moore, "Freezing and Melting in Finite Media, With an Assessment of Molten Fuel Containment Capability of the SLSF," *Journal of Nuclear Engineering and Design, 56*, 1980, pp. 413-428.

8. M. S. El-Genk, "On a Vapor Explosion in the RIA-ST-4 Experiment," *Transactions of the American Nuclear Society Annual Meeting. Las Vegas, Nevada, June 8-13, 1980.*

9. R. W. Ohse et al., "Extension of Vapor Pressure Measurements of Nuclear Fuel (U, Pu)O_2 and UO_2 to 7000 K for Fast Reactor Safety Analysis," *Journal of Nuclear Materials, 59*, 1976, pp. 112-124.

10. J. A. McClure, *Particle Size Distributions from Fuel Rods Fragmented During Power Burst Tests in the Capsule Driver Core*, IN-1428, October 1970.

11. R. E. Pawel, J. V. Cathcart, and R. A. McKee, "The Kinetics of Zircaloy-4 in Steam at High Temperatures," *Journal of Electrochemical Science and Technology, 126*, 1979, pp. 1105-1111.

12. R. C. Ballinger, W. G. Dobson, and R. R. Biederman, "Oxidation Reaction Kinetics of Zircaloy-4 in an Unlimited Steam Environment," *Journal of Nuclear Materials, 62*, 1976, pp. 213-270.

13. A. W. Cronenberg and M. S. El-Genk, "An Assessment of Oxygen Diffusion During UO_2-Zircaloy Interaction," *Journal of Nuclear Materials, 78*, 1978, pp. 390-407.

14. P. Hofmann and C. Politis, "The Kinetics of the Uranium Dioxide-Zircaloy Reactions at High Temperatures," *Journal of Nuclear Materials, 87*, 1979, pp. 375-397.

15. E. E. Anderson, "Radiative Heat Transfer in Molten UO_2 Based on the Rosseland Diffusion Method," *Journal of Nuclear Technology, 30*, 1976, p. 65.

16. D. H. Cho, S. H. Chan, and G. M. Hauser, "Radiative Heat Transfer in a Horizontal Molten Fuel Layer with Volumetric Heating," *Transactions of the American Nuclear Society, 30*, 1978, p. 473.

17. S. H. Chan, F. B. Cheung, and D. H. Cho, "The Effect of Radiation Heat Transfer on Maximum Nonboiling Thickness of a Molten Oxide Fuel Layer with Decay Heating," *Transactions of the American Nuclear Society, 33*, November 1979, p. 521.

18. R. L. Gorring and S. W. Churchill, "Thermal Conductivity of Heterogeneous Materials," *Chemical Engineering Progress, 57*, 1961, pp. 53-59.

19. W. F. Ames, *Nonlinear Partial Differential Equations in Engineering*, New York: Academic Press, 1965.

20. D. L. Hagrman and G. A. Reymann, *MATPRO - Version 11, A Handbook of Material Properties for Use in the Analysis of Light Water Reactor Fuel Rod Behavior*, NUREG/CR-0497, TREE-1280, February 1979.

APPENDIX A

RADIATIVE COOLING AT THE MOLTEN DEBRIS LAYER SURFACE

APPENDIX A

RADIATIVE COOLING AT THE MOLTEN DEBRIS LAYER SURFACE

The inner surface of the test shroud wall was coated by a molten debris layer, having a thickness of 0.7 mm, upon fuel rod failure in the RIA-ST-4 experiment. This molten debris layer was cooled by two means; transient heat conduction through the shroud wall, and radiative cooling at the surface of the debris layer to the water vapor within the flow shroud. A net radiative exchange coefficient, h_R, at the debris layer surface was employed in the analysis to evaluate the effect of cooling by radiation on the transient freezing of the molten debris layer. An estimate of h_R is obtained in this appendix by considering the following simplifying assumptions:

1. The water vapor within the shroud is at a constant temperature equal to the saturation temperature (554 K).

2. The partial pressure of the water vapor, P_v, is equal to the total coolant pressure, P_T, that is, $P_v = 6.45$ MPa. Contributions to the system pressure by fission gases released upon fuel failure and the gases produced by the steam reaction with the debris are neglected.

3. The flow shroud is treated as a long cylinder of inner diameter, D_i, where

$$D_i = (D_o - 2\delta) \simeq 17.9 \text{ mm} \quad \text{(A-1)}$$

where D_o is the flow shroud inner diameter before the test (19.3 mm), and δ is the debris layer thickness (0.7 mm).

4. A unity radiative view factor is assumed.

5. The emissivity of the debris, ε_f, is taken to be equal to that of the UO_2 fuel[A-1] (~ 0.4083).

6. The emissivity of the debris, ε_f, and the effective emissivity of the water vapor, ε_v, are assumed constant during the analysis.

7. The water vapor effective absorptivity, ε_v, is given by the relation[A-2]

$$\varepsilon_v = \varepsilon_{av} \left(\frac{4 + a + b - c}{4}\right) \quad \text{(A-2)}$$

where c is an exponent used in evaluating the vapor absorptivity, and is equal to 0.45 for water vapor.[A-2] The coefficients a and b are determined from Figure 4-18 in Reference A-2, and ε_{av} is the water vapor average absorptivity, which depends on the vapor temperature and the product of $P_v\ell$, and the system total pressure, $P_T(P_v \simeq P_T)$. The parameter ℓ is the mean beam length, which is equal to 0.9 D_i (see Table 4-2 in Reference A-2). The coefficients a and b, as well as ε_{av}, are evaluated at an average temperature, T_{av}, of 2000 K, which is the arithmetic average of the water vapor saturation temperature (544 K) and the temperature of the molten debris at the time of fuel failure ($\sim$3500 K).

The net radiation heat flux, q_R, at the surface of the molten debris layer is calculated from the relation

$$q_R = h_R \left(T_a(t) - T_{sat}\right) \quad \text{(A-3)}$$

where h_R is the net radiative exchange coefficient, T_{sat} is the water vapor saturation temperature corresponding to the system pressure (6.45 MPa), and T_a is the temperature at the surface of the debris layer, which varies with time. The temperature T_a is initially equal to 3500 K. The net radiative exchange coefficient, h_R, in Equation (A-3) is calculated from the relation

$$h_R = \frac{\sigma_{sB}}{\frac{1}{\varepsilon_f} + \frac{1}{\varepsilon_v} - 1} \left(\frac{T_a^4(t) - T_{sat}^4}{T_a(t) - T_{sat}}\right) \quad \text{(A-4)}$$

where σ_{sB} is the Stefan-Boltzmann constant (5.67×10^{-8} W/m^2·K^4).

To calculate h_R, the effective absorptivity of water vapor ε_v, was assessed in the following manner. Since the mean beam length, ℓ, is equal to 0.9 x diameter (see Table 4-2 of Reference A-2) for a long tube (Assumption 3), then $P_v\ell$ = 3.4 ft-atm (Assumption 2). At T_{av} = 3600°R (Assumption 7), the gas absorptivity ε_w (from Figure 4-15 of Reference A-2) ≃ 0.2, and (from Figure 4-16 of Reference A-2), the correction factor c_w ≃ 1.3. Therefore, the average absorptivity of the water vapor ε_{av} = (0.2 x 1.3) = 0.26. Using Figure 4-18 of Reference A-2 for H_2O, the coefficients a and b ≃ 0.4 and ≃ -1.2, respectively. With the coefficient c = 0.45 for water vapor,[A-2] the effective thermal absorptivity of the water vapor, ε_v, is then calculated, using Equation (A-2), as

$$\varepsilon_v = 0.26 \left(\frac{4 + 0.4 - 1.2 - 0.45}{4}\right)$$

$$\simeq 0.18.$$

The net radiative exchange coefficient, h_R, at the surface of the debris layer is then calculated through the use of Equation (A-4). Note that h_R varies with time because the temperature at the debris layer surface, T_a, is a function of time.

REFERENCES

A-1. D. L. Hagrman and G. A. Reymann, *MATPRO - Version 11, A Handbook of Material Properties for Use in the Analysis of Light Water Reactor Fuel Rod Behavior*, NUREG/CR-0497, TREE-1280, February 1979.

A-2. W. H. McAdams, *Heat Transmission*, New York: McGraw-Hill Book Company, 1954.

APPENDIX B

AN ESTIMATE OF THE HEAT TRANSFER COEFFICIENTS AT THE SHROUD WALL OUTER SURFACE

APPENDIX B

AN ESTIMATE OF THE HEAT TRANSFER COEFFICIENTS AT THE SHROUD WALL OUTER SURFACE

In the calculations performed in the present work, two modes of heat transfer are considered to occur at the RIA-ST-4 shroud wall outer surface during the transient freezing of the molten debris on the inner surface of the wall. These modes are forced convection heat transfer and stable film boiling heat transfer. During the former mode, in which the wall surface temperature is assumed to be less than the critical temperature of the water (647 K), the convective heat transfer coefficient at the wall outer surface, h_c, is calculated using the Dittus-Boelter correlation.[B-1]

$$\frac{h_c D}{k_\ell} = 0.023 \left(\frac{\rho_\ell v D}{\mu_\ell}\right)^{0.8} \left(\frac{\mu_\ell C_\ell}{k_\ell}\right)^{0.4} \quad \text{(B-1)}$$

where D is the equivalent hydraulic diameter of the bypass flow tube and v is the inlet velocity of the coolant bypass flow. The thermophysical properties of the water, ρ_ℓ, k_ℓ, C_ℓ, and μ_ℓ, are evaluated at the coolant bulk temperature (538 K). In the RIA-ST-4 experiment the inlet velocity of the coolant bypass flow, v, was about 0.42 m/s. The value of h_c calculated from Equation (B-1) is taken to be constant during the first mode of heat transfer (that is, convective cooling).

When the wall surface temperature, T_b, reaches or exceeds the critical temperature of the coolant ($T_{crit} \simeq 647$ K), stable film boiling is assumed to occur at the outer surface of the wall. In such a case, the heat flux at the wall surface, q, is calculated by the simple relation

$$q = h_B \, \Delta T \quad \text{(B-2)}$$

where ΔT is the difference between the wall temperature, T_b, which is a function of time, and the saturation temperature of the water T_{sat} (~544 K at 6.45 MPa); and h_B is the total film boiling heat transfer coefficient, given here in terms of conduction and radiation coefficients, h_{co} and h_r, respectively. Bromley[B-2] proposed the following approximate relationships between h_B, h_{co}, and h_r:

$$h_B = h_{co} + \frac{3}{4} h_r \quad \text{(when } h_{co} > h_r\text{)} \quad \text{(B-3a)}$$

$$h_B = h_{co} + h_r \left\{ 0.75 + \left[\frac{0.25 \left(\frac{h_r}{h_{co}}\right)}{2.62 + \left(\frac{h_r}{h_{co}}\right)} \right] \right\}$$

$$\text{(when } h_{co} \le h_r\text{)}. \quad \text{(B-3b)}$$

The conduction term, h_{co}, in Equation (B-3) is calculated from the following correlation of Ellion:[B-3]

$$h_{co} = 0.714 \left[\frac{k_v^3 \rho_v \rho_c h_{fg} g}{H \mu_v (T_b - T_{sat})} \right]^{0.25} \quad \text{(B-4)}$$

where ρ_v, k_v, and μ_v are the vapor density, thermal conductivity, and viscosity, respectively; h_{fg} is the coolant latent heat of vaporization; ρ_c is the coolant density; g is the acceleration of gravity; and H is the boiling length along the wall surface. The boiling length is taken to be 1 m, which is approximately equal to the axial extension of the deposited molten fuel debris layer along the inner surface of the shroud wall. The value of h_{co} calculated from Equation (B-4) is an average value over the boiling length, H. Ellion[B-3] has developed some experimental data to substantiate his correlation given by Equation (B-4). The predictions were in reasonable agreement with the experiment data. These data were obtained for forced flow of water through an annulus composed of an inner heated tube, 0.635 cm in diameter and 7.62 cm long, and outer, adiabatic tube, 6.35 cm in diameter. The coolant pressure ranged from 0.109 to 0.41 MPa, the coolant subcooling from 27.7 to 55.5 K, and the coolant upward velocity from 0.335 to 1.524 m/s.

The contribution by thermal radiation across the vapor film, h_r, to the total film boiling heat

transfer coefficient, h_B, is calculated by the following equation for radiation between two parallel plates:

$$h_r = \frac{\sigma_{sB}}{\frac{1}{\varepsilon_w} + \frac{1}{\varepsilon_\ell} - 1} \left(\frac{T_b^4(\varepsilon) - T_{sat}^4}{T_b(t) - T_{sat}} \right) \quad \text{(B-5)}$$

where σ_{sB} is the Stefan-Boltzmann constant (5.67×10^{-8} W/m^2·K^4); and ε_w and ε_ℓ are the emissivity of the wall material and the absorptivity of the coolant, respectively.

Figure B-1 is a plot of the different coefficients of heat transfer at the outer surface of the shroud wall. The lowest curve in Figure B-1 is the radiative heat transfer coefficient across the vapor film, h_r, using a value of 0.8 for the emissivity of zircaloy (ε_w) and 0.966 for the water absorptivity (ε_ℓ). The intermediate curve is the conduction component of heat transfer, h_{co}, which would be expected if there were no radiation [Equation (B-4)]. The upper curve, represented by a solid line, is the total film boiling heat transfer coefficient, h_B. This coefficient includes the combined contribution of both radiation and conduction. The solid horizontal line to the left, for $T_b < T_{crit}$ (647 K), represents the forced convection heat transfer, h_c, calculated using Equation (B-1). As shown in Figure B-1, the film boiling heat transfer coefficient, h_B, does not change significantly as the wall surface temperature, T_b, increases until it reaches or exceeds 1600 K ($T_b - T_{sat} \simeq 1056$ K). At or above that temperature, the contribution to h_B by the thermal radiation, h_r, becomes significant and outweighs that due to conduction, h_{co}.

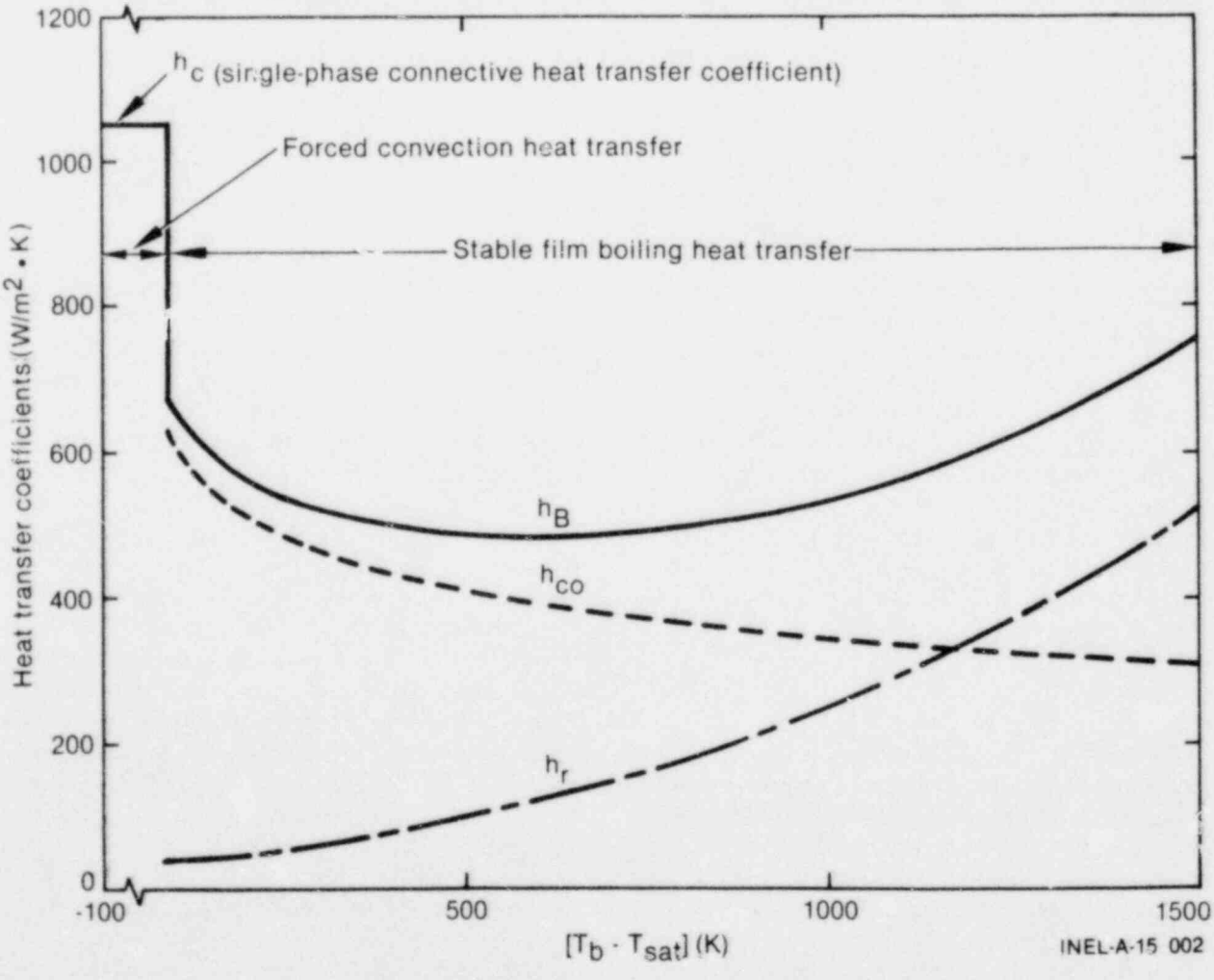

Figure B-1. Coefficient of heat transfer at the shroud outer surface.

REFERENCES

B-1. W. H. McAdams, *Heat Transmission*, New York: McGraw-Hill Book Company, 1954.

B-2. L. A. Bromley, "Heat Transfer in Stable Film Boiling," *Chemical Engineering Progress, 46*, 1950, pp. 221-227.

B-3. D. P. Jordan, "Film and Transition Boiling," *Advances in Heat Transfer, 5* , 1968, pp. 55-128.

APPENDIX C

ACCURACY OF THE FINITE ELEMENT COMPUTER CODE SINGLE

APPENDIX C

ACCURACY OF THE FINITE ELEMENT COMPUTER CODE SINGLE

Examined in this appendix is the accuracy of the computer code SINGLE in solving one-dimensional transient heat conduction problems with a change of phase. The code calculations are compared with closely related exact solutions.[C-1,C-2] These exact solutions, however, pertain to much less general change-of-phase problems than that explicitly treated in the present work, because the exact analytical solutions to most problems of transient heat conduction with a moving phase transformation boundary(ies) are not readily obtainable. The difficulty arises from the always present nonlinear boundary condition(s) due to a phase change, and in addition, the governing equations themselves become nonlinear when temperature-dependent thermophysical properties are considered, which is the case in the present analysis.

The accuracy of the SINGLE code is assessed when applied to the growth[C-1] of a solidified crust in a stagnant, superheated liquid on an isothermal wall (classical Neumann problem[C-1]) and on a semi-infinite wall which melts simultaneously.[C-2] For such problems,[C-1,C-2] the temperature of the interface between the solidified crust and the wall is constant with time. Therefore, the instantaneous frozen crust thickness, $\delta(t)$ can be represented by the relation

$$\delta(t) = 2\lambda_s \sqrt{\alpha_s t} \qquad \text{(C-1)}$$

where α_s is the thermal diffusivity of the frozen crust, and λ_s is the freezing coefficient. When the wall is isothermal,[C-1] λ_s is obtained by solving the following transcendental equation:[C-1]

$$\frac{e^{-\lambda_s^2}}{\operatorname{erf}(\lambda_s)} - \frac{\sigma\,\Theta_b\, e^{-(\beta^2\,\lambda_s^2)}}{\operatorname{erfc}(\lambda_s\ \beta)} - \lambda_s\sqrt{\pi}/SN = 0 \qquad \text{(C-2)}$$

where σ is the freezing liquid-crust thermal ratio; SN is the Stefan number for freezing; β is a thermal diffusivity ratio; and Θ_b is the dimensionless bulk temperature of the liquid, which are given by the relations

$$\sigma = (\rho_\ell\ C_\ell\ k_\ell / \rho_s\ C_s\ k_s)^{1/2}$$

$$SN = C_s\ (T_f - T_o)/L_s$$

$$\beta = (\alpha_s/\alpha_\ell)^{1/2}$$

$$\Theta_b = (T_b - T_f)/(T_f - T_o) \qquad \text{(C-3)}$$

where ρ_ℓ, C_ℓ, k_ℓ and ρ_s, C_s, and k_s are density, heat capacity, and thermal conductivity of the freezing liquid and the crust, respectively; α_ℓ is the thermal diffusivity of the liquid; T_b and T_f are the bulk and the fusion temperatures of the liquid; T_o is the isothermal wall temperature; and L_s is the latent heat of fusion.

For freezing on a semi-infinite wall which melts simultaneously,[C-2] the instantaneous thickness of the frozen crust is still described by Equation (C-1), whereas the thickness of the wall molten layer, $\delta_m(t)$, is given by the relation

$$\delta_m(t) = 2\,\lambda_m\,\sqrt{\alpha_m t} \qquad \text{(C-4)}$$

where α_m is the thermal diffusivity of the wall molten layer and λ_m is the wall melting coefficient. In the latter case, the freezing and melting coefficients (λ_s and λ_m) are obtained through a simultaneous solution of the following two transcendental equations (provided in the box at the top of the next page):[C-2]

$$\left[\frac{\sigma_m}{\exp(\lambda_s^2)\ \mathrm{erf}(\lambda_m) + \sigma_m \exp(\lambda_s^2)\ \mathrm{erf}(\lambda_s)}\right] - \left[\frac{\Theta_1}{\exp(\beta_1^2\lambda_s^2)\ \mathrm{erfc}(\beta_1\lambda_s)}\right] = \lambda_s \sqrt{\pi}/SN^* \quad \text{(C-5)}$$

and

$$\left[\frac{1}{\sigma_m \exp(\lambda_m^2)\ \mathrm{erf}(\lambda_s) + \exp(\lambda_m^2)\ \mathrm{erf}(\lambda_m)}\right] - \left[\frac{\Theta_2}{\exp(\beta_2^2\lambda_m^2)\ \mathrm{erfc}(\beta_2\lambda_m)}\right] = \lambda_m \sqrt{\pi}/SN_m \quad \text{(C-6)}$$

where σ_m is the wall molten layer to frozen crust thermal ratio; SN^* and SN_m are Stefan numbers for liquid freezing and wall melting, respectively; β_1 and β_2 are thermal diffusivities ratios; and Θ_1 and Θ_2 are dimensionless temperatures. The terms σ_m, SN^*, SN_m, β_1, β_2, Θ_1, and Θ_2 are given here as

$$\sigma_m = (\rho_m C_m k_m / \rho_s C_s k_s)^{1/2},$$

$$SN^* = C_s (T_f - T_{mp})/L_s,$$

$$SN_m = C_m (T_f - T_{mp})/L_m,$$

$$\beta_1 = \left(\frac{\alpha_s}{\alpha_\ell}\right)^{1/2},$$

$$\beta_2 = \left(\frac{\alpha_m}{\alpha_w}\right)^{1/2},$$

$$\Theta_1 = \sigma \left(\frac{T_b - T_f}{T_f - T_{mp}}\right),$$

$$\Theta_2 = \sigma_w \left(\frac{T_{mp} - T_o}{T_f - T_{mp}}\right),$$

$$\sigma_w = (\rho_w C_w k_w / \rho_m C_m k_m)^{1/2}, \quad \text{(C-7)}$$

where σ_w is the solid wall to wall molten layer thermal ratio; α_w ρ_w, C_w, and k_w are the solid wall thermal diffusivity, density, specific heat, and thermal conductivity, respectively; T_{mp} is the wall melting point; T_o is the initial temperature of the wall; and L_m is the wall latent heat of melting.

Freezing on an Isothermal Wall

The freezing coefficient, λ_s, of a stagnant, superheated liquid on an isothermal wall, as calculated by the exact solution [Equation (C-2)] and the computer code SINGLE, is plotted versus the Stefan number of freezing in Figure C-1. As indicated, λ_s increases as the Stefan number of freezing is increased. For small values of SN (that is, a large latent heat of fusion), the freezing coefficient is small, indicating a slow freezing process. When SN is large (that is, a small latent heat of fusion), the freezing process is fast, since less heat is liberated upon liquid freezing.

As shown in Figure C-1, the code calculations are in good agreement with the exact solution, especially at low values of Stefan number (that is, slow freezing processes). The code predictions are accurate to within 2% of the exact solution.

Stefan numbers of freezing divided by the heat capacity of the solid, for molten UO_2 and molten zircaloy, are plotted in Figure C-2 versus the isothermal wall temperature. Note that the ranges of SN for UO_2 and for zircaloy are up to 3.5 and 2.7 respectively, depending on the wall temperature, T_o, and the heat capacity of the solidified crust. In the following subsection, the code predictions for the freezing and melting coefficients, λ_s and λ_m, are compared with the exact solution (Equations C-5 and C-6) for the freezing of a stagnant, superheated liquid on a semi-infinite wall which melts simultaneously.[C-2]

Freezing on a Simultaneously Melting Wall

Figure C-3 presents a comparsion between the exact solution and the SINGLE code in calculating

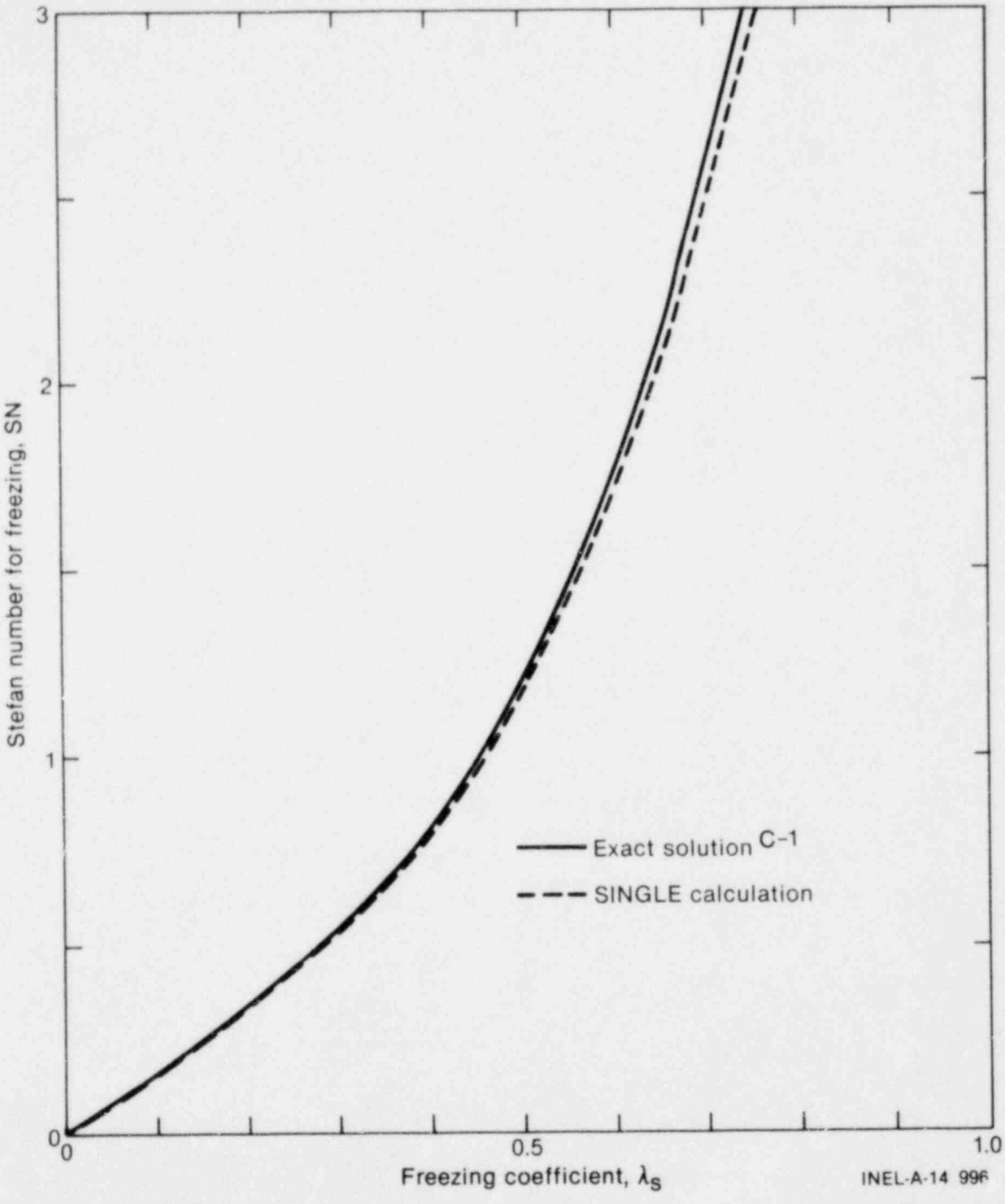

Figure C-1. Accuracy of the SINGLE code in calculating the freezing coefficient of a superheated liquid on an isothermal wall.

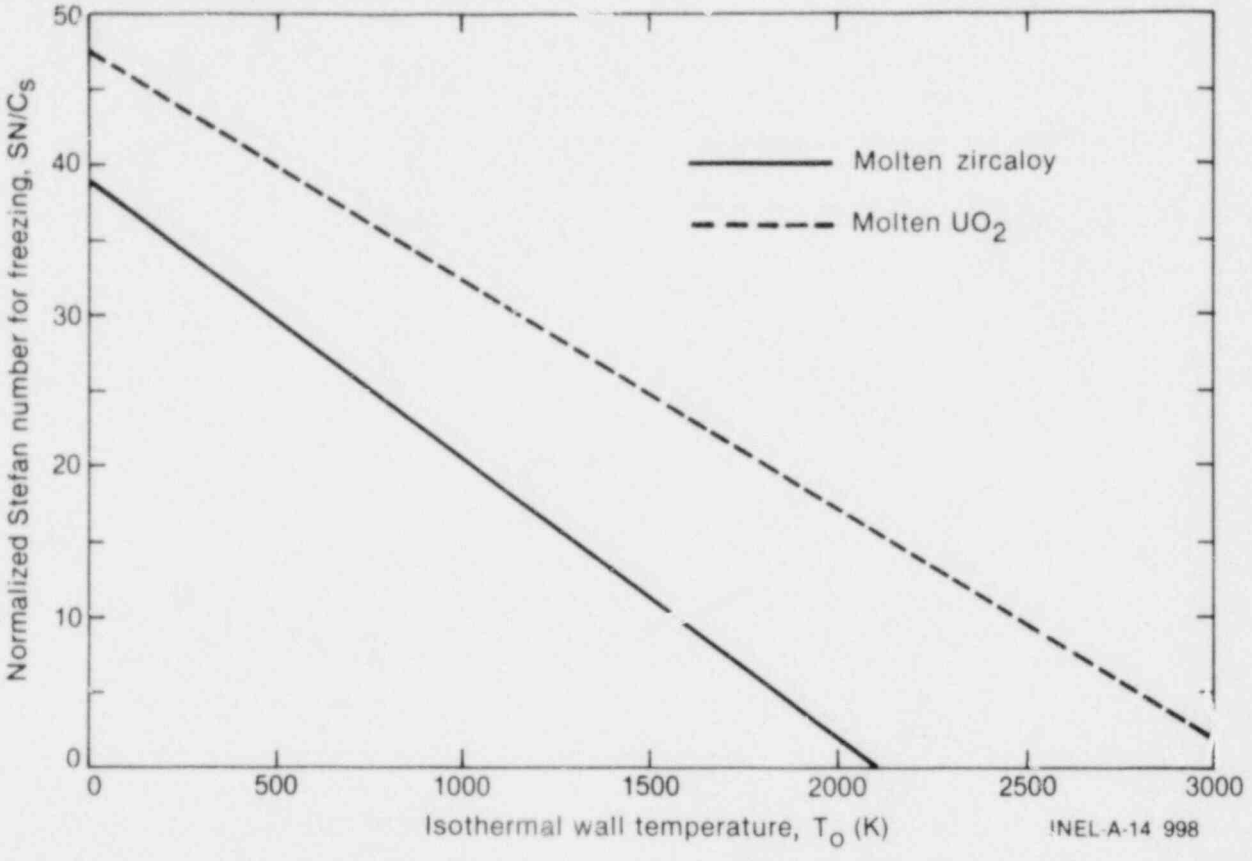

Figure C-2. Stefan number for freezing of molten UO_2 and molten zircaloy as functions of wall temperature.

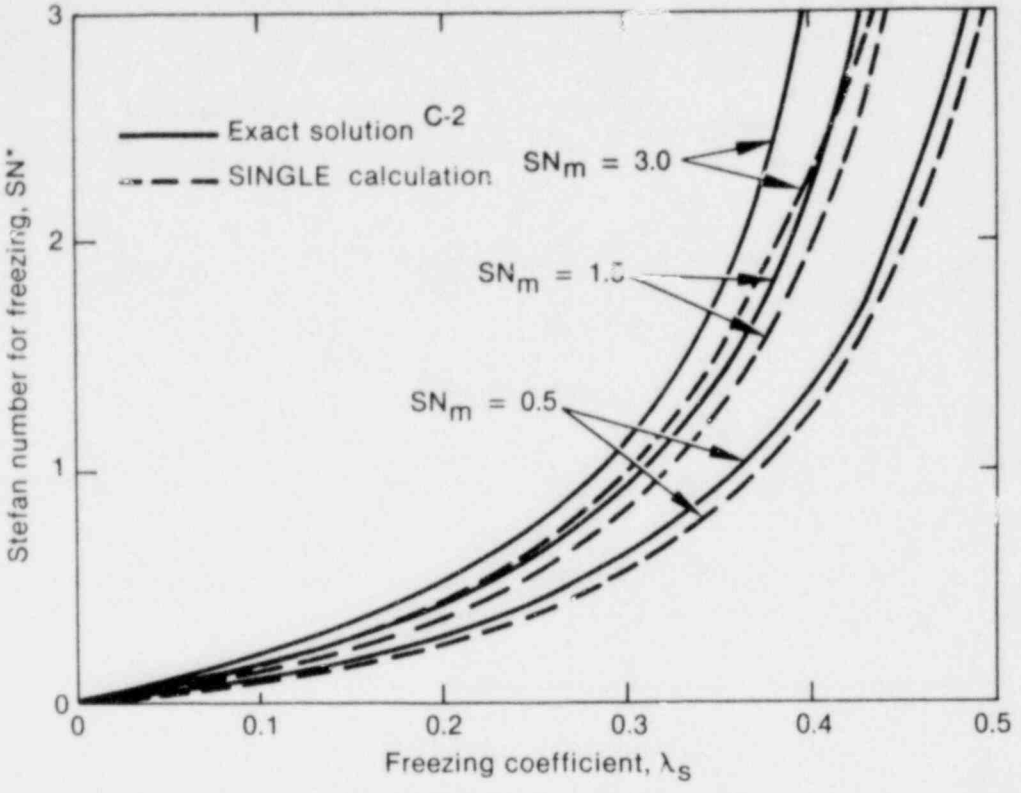

(a) Freezing coefficient

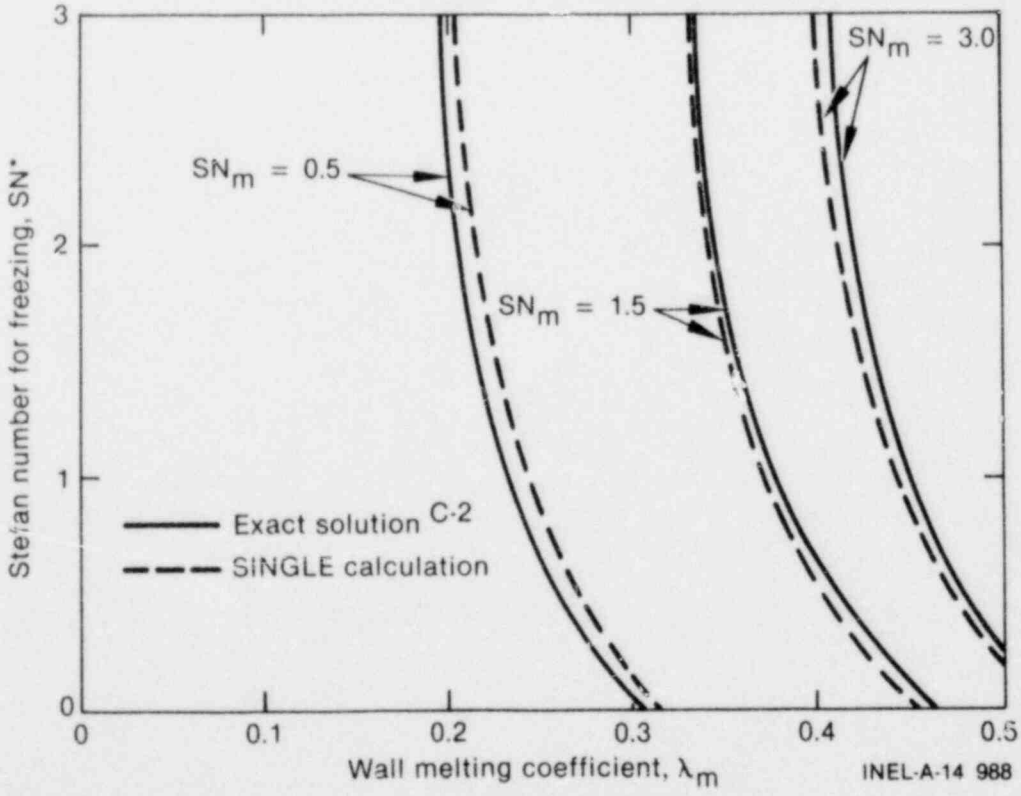

(b) Melting coefficient

Figure C-3. Accuracy of the SINGLE code in calculating the freezing and melting coefficients of a stagnant, superheated liquid on a semi-infinite wall which melts simultaneously.

the liquid freezing and wall melting coefficients, λ_s and λ_m, respectively. These calculations are performed for $\sigma = \sigma_w = 1$, $\beta_1 = \beta_2 = 1$, and $\theta_1 = \theta_2 = 0.5$, for simplicity. In Figure C-3(a), the Stefan number of freezing, SN^*, is plotted versus the freezing coefficient, $_s$, for different values of the Stefan number of wall melting, SN_m. As indicated, the code predictions are within 9% of the exact solution. Note that the accuracy of the code improves as SN^* is decreased (a slow freezing process), or upon reducing SN_m (a slow melting process in the wall). The accuracy of the code for calculating the wall melting coefficient λ_m is demonstrated in Figure C-3(b), where the Stefan number of freezing is plotted versus λ_m for different values of SN_m. As indicated, the code predictions are within 3% of the exact solution. Note that SN^* and SN_m are about 1.5 and 2.9 for molten UO_2 freezing and zircaloy wall melting, respectively.

REFERENCES

C-1. H. S. Carslaw and J. C. Jaeger, *Conduction of Heat in Solids*, 2nd edition, Oxford: Clarendon Press, 1959.

C-2. M. Epstein, "Heat Conduction in the UO_2-Cladding Composite Body with Simultaneous Solidification and Melting," *Journal of Nuclear Science and Engineering, 51*, 1973, pp. 84-87.